

UNIVERSIDAD SAN FRANCISCO DE QUITO USFQ

Colegio de Posgrados

**Gain enhanced metal nano-shells:
electromagnetic response and thermal
behavior, below and above the emission
threshold**

Milena Sophia Mora Chaguay

Alessandro Veltri, Ph.D. & Maria Antonia Iatì, Ph.D
Directores del Trabajo de Titulación

Maestría en Física

Trabajo de titulación presentado como requisito para la obtención del
título de Magister en Física

Quito, 1 de Diciembre de 2023

UNIVERSIDAD SAN FRANCISCO DE QUITO

USFQ

Colegio de Posgrados

HOJA DE CALIFICACIÓN DE TRABAJO DE TITULACIÓN

Gain enhanced metal nano-shells: electromagnetic response and thermal behavior, below and above the emission threshold

Milena Sophia Mora Chaguay

Calificación:

Nombre del profesor, Título académico: Alessandro Veltri, Ph.D. & Maria Antonia Iati, Ph.D

Firma del profesor

Firma del profesor

Quito, 1 de Diciembre de 2023

Derechos de Autor

Por medio del presente documento certifico que he leído todas las Políticas y Manuales de la Universidad San Francisco de Quito USFQ, incluyendo la Política de Propiedad Intelectual USFQ, y estoy de acuerdo con su contenido, por lo que los derechos de propiedad intelectual del presente trabajo quedan sujetos a lo dispuesto en esas Políticas. Asimismo, autorizo a la USFQ para que realice la digitalización y publicación de este trabajo en el repositorio virtual, de conformidad a lo dispuesto en el Art. 144 de la Ley Orgánica de Educación Superior.

Nombres y apellidos: Milena Sophia Mora Chaguay

Código: 00329961

Cédula de Identidad: 1724810609

Lugar y fecha: Quito, 1 Diciembre de 2023

ACLARACIÓN PARA PUBLICACIÓN

Nota: El presente trabajo, en su totalidad o cualquiera de sus partes, no debe ser considerado como una publicación, incluso a pesar de estar disponible sin restricciones a través de un repositorio institucional. Esta declaración se alinea con las prácticas y recomendaciones presentadas por el Committee on Publication Ethics COPE descritas por Barbour et al. (2017) Discussion document on best practice for issues around theses publishing, disponible en <http://bit.ly/COPETheses>.

UNPUBLISHED DOCUMENT

Note: The following capstone project is available through Universidad San Francisco de Quito USFQ institutional repository. Nonetheless, this project – in whole or in part – should not be considered a publication. This statement follows the recommendations presented by the Committee on Publication Ethics COPE described by Barbour et al. (2017) Discussion document on best practice for issues around theses publishing available on <http://bit.ly/COPETheses>.

Para Lennon, Janis, Alanis, Copérnico y Kora.

Agradecimientos

En primer lugar quiero agradecer a mi tutor Alesandro Veltri, gracias por creer en mi, por tu paciencia y por todas tus enseñanzas. Mi vida cambió luego de explorar el mundo de la física a tu lado. También, quiero agradecer a Antonella Iatì y Onofrio Marago, por acogerme y cuidarme en mi estadía en Italia. A pesar de estar muy lejos me hicieron sentir como en casa.

A mis profesores de física, con un reconocimiento especial a Melissa Infusino. Tu forma de instruir hizo una gran diferencia en mi aprendizaje.

A mis compañeros de la maestría, al equipo de NanoSoftlab y a mis amigos. Particularmente a Adrian Vázquez, Jose Ignacio Palacios, Alejandro Ruedra y Ariana Soria.

A Mateo Martínez, por creer en mí incluso cuando yo no lo hago, por tu paciencia y apoyo constante. Me siento afortunada de que seas parte de mi vida.

A mi familia, por ser mi soporte, mi guía y mi fuente motivación. Gracias por su apoyo incondicional. Y por último, a Kora y Alanis, gracias por llenar mi vida de alegría.

Resumen

En esta tesis se presentan dos formas de modelar el comportamiento electromagnético de una partícula plasmónica tipo nano-shell, que son la aproximación cuasiestática y la teoría de Mie. Este análisis conduce a la discusión de la ruptura del régimen cuasiestático debido al aumento del tamaño de la nanopartícula, la cantidad de metal presente en la partícula y la ganancia inyectada en el sistema. Además, en busca de homogeneizar diversas configuraciones resueltas con el mismo tratamiento matemático, se formula un sistema modular para las ecuaciones dependientes del tiempo. Para lograr esto, se define una matriz de coeficientes derivada de las condiciones de contorno del sistema estudiado, de esta manera, sistemas tan distintos como una esfera única en un medio de ganancia uniforme y una nano-shell pueden deducirse a una ecuación diferencial lineal acoplada. Además, se extiende el modelo de Baffou para los efectos de calentamiento en una nanopartícula metálica esférica a una partícula tipo nano-shell. Se obtiene que mediante el uso de una nano-shell en lugar de una nanoesfera es posible alcanzar temperaturas más altas utilizando partículas del mismo tamaño. Para compensar las pérdidas por absorción, se añaden especies activas al núcleo de la nanopartícula, las cuales son bombeadas con una fuente externa. Permitiendo modular la cantidad deseada de calentamiento en la nanopartícula. Por último, se presenta una aplicación directa en la eficiencia de una trampa óptica, resultando que al inyectar ganancia en el sistema de trampa es posible obtener pinzas ópticas más eficientes que aumentando la potencia láser.

Palabras clave: Plasmónica, nano-shell, aproximación cuasiestática, teoría de Mie, comportamiento térmico, medio de ganancia, trampa óptica.

Abstract

In this thesis are presented two ways of modeling the electromagnetic behavior of a plasmonic nano-shell particle, which are the quasistatic approximation and the Mie theory. This analysis leads to the discussion of the rupture of the quasistatic regime by the increase of the size of the nanoparticle, the amount of metal that has the particle and the gain pumped into the system. Furthermore, looking for homogenize various configurations that are solved with the same mathematical treatment, it is formulated a modular system for the time dependent equations. In order to do this, it is defined a coefficients matrix derived from the boundary conditions of the studied system, in this way, system as different as a single sphere in a uniform gain medium and a nano-shell can be deduced to a linear coupled differential equation. Additionally, it is extended the Baffou model for the heating effects in a spherical metal nanoparticle to a nano-shell particle. Obtaining that by using a nano-shell particle instead of a nanosphere it is possible to achieve higher temperatures using particles of the same size. In order to compensate the absorption losses, there are added active species into the core of the nanoparticle, which are pumped with an external source. Allowing to modulate the desired amount of heating in the nanoparticle. Lastly, it is presented a direct application in the efficiency of an optical trap, resulting that by pumping gain into the trapping system it is possible to obtaining high efficient tweezers than by increasing the laser power.

Keywords: Plasmonics, nano-shell particle, quasistatic approximation, Mie theory, thermal behavior, gain medium, optical trap .

Contents

List of Figures	11
1 Introduction	14
1.1 Plasmonics	14
1.1.1 Localized Surface Plasmon Resonance	16
1.2 Thermo-plasmonics	17
1.2.1 Plasmonic Photothermal Therapy	17
1.2.2 Optical trap efficiency	19
2 Choosing the right nanoparticle	22
2.1 Gain enhanced nano-shell	23
2.1.1 The Gain assisted Medium	23
2.1.2 The Metal	28
2.1.3 The Solvent	31
3 Electromagnetic model	32

	10
3.1 The coated sphere	32
3.2 Quasistatic Approximation	33
3.2.1 Cross Sections	38
3.3 Mie Theory	40
3.3.1 Cross Sections	51
3.4 Rupture of the quasistatic limit	52
4 Time dependent model	56
4.1 Below the Emission Threshold	64
4.2 Above the Emission Threshold	65
5 Thermal Behavior	72
5.1 Heat dissipated by a nanoparticle	72
5.2 Temperature in a nanosphere	73
5.3 Temperature in a nano-shell	75
6 Trapping behavior	85
7 Conclusions	94
References	95

List of Figures

1.1	Notre Dame Cathedral: stained-glass rose window	15
2.1	Coated sphere.	22
2.2	Complex permittivity for gold, calculated using a free electron model and including additional losses through the interpolation of the data measured by Johnson and Christy.	30
3.1	A sphere of permittivity ε_1 , in a shell of permittivity ε_2 in a host of permittivity ε_3	32
3.2	Absorption Cross Section for a nano-shell particle with $\rho = 0.8$ and $G = 0$, in which $\lambda = 590[nm]$ is fixed.	52
3.3	Absorption Cross Section for a nano-shell particle with external radius of $40 [nm]$ and $\rho = 0.8$, in which $\lambda = 626[nm]$ is fixed and G is below the emission threshold.	54
4.1	Analytical and Numerical solutions calculated for $\hbar\omega = 2.811$ eV with a sub-emissive gain quantity ($G = 0.033$). The pump is switched on at $t = 10$ ps. We present the real and imaginary part of: (a) q_0 ; (b) q_1 ; (c) q_2 . The numerical solutions are presented in continuous lines (red and black respectively for the real and imaginary part) while the analytical solutions are presented in dashed lines (purple and brown respectively for the real and imaginary part).	68

- 4.2 Normalized polarizability with a sub-emissive gain quantity ($G = 0.033$). The real and imaginary parts are shown as black and orange lines, respectively. (a) Time dependence calculated for $\hbar\omega = 2.811$ eV. (b) Steady-state spectrum. A blue line at $\hbar\omega = 2.811$ eV serves as a reference. 69
- 4.3 Analytical and Numerical solutions at $\hbar\omega = 2.811$ eV with a super-emissive gain quantity ($G \sim 0.136$). The pump is switched on at $t = 10$ ps. Time evolution for the real and imaginary part of: (a) q_0 ; (b) q_1 ; (c) q_2 . The numerical solutions are presented in continuous lines (red and black respectively for the real and imaginary part) while the analytical solutions are presented in dashed lines (purple and brown respectively for the real and imaginary part). 70
- 4.4 Normalized polarizability with a super-emissive gain quantity ($G \sim 0.136$). The real and imaginary parts are shown as black and orange lines, respectively. (a) Time dependence calculated for $\hbar\omega = 2.811$ eV. (b) Steady-state spectrum. A blue line at $\hbar\omega = 2.811$ eV serves as a reference. 71
- 5.1 Temperature inside and outside a gold nanoparticle with radius 10 [nm] in the spectrum from 1.5 [eV] to 3 [eV], also we present the temperature in function of the radial distance for 2.639324 [eV] (dark pink line) and 2.339324 [eV] (cyan line) 74
- 5.2 Temperature inside and outside a nano-shell particle with silica core embedded by gold with external radius 10 [nm] and $\rho = 0.4$ in the spectrum from 1.5 [eV] to 3 [eV], also we present the temperature in function of the radial distance for 2.63326 [eV] (dark pink line) and 2.33326 [eV] (cyan line) 81
- 5.3 Temperature inside and outside a nano-shell particle with silica core embedded by gold with external radius 10 [nm] and $\rho = 0.6$ in the spectrum from 1.5 [eV] to 3 [eV], also we present the temperature in function of the radial distance for 2.50974 [eV] (dark pink line) and 2.20974 [eV] (cyan line) 82

5.4	Temperature inside and outside a nano-shell particle with silica core embedded by gold with external radius 10 [nm] and $\rho = 0.8$ in the spectrum from 1.5 [eV] to 3 [eV], also we present the temperature in function of the radial distance for 2.18608 [eV] (dark pink line) and 1.88608 [eV] (cyan line)	83
6.1	Radial and axial components of the optical force, power dissipated as heat of a passive silica-silver nano-shell of radius $a_2 = 20$ [nm] for $P = 50$ [mW] (upper row), $P = 120$ [mW] (middle row) and $P = 2000$ [mW] (lower row).	91
6.2	Radial and axial components of the optical force, power dissipated as heat of a gain enhanced silica-silver nano-shell at $P = 50$ [mW] for $G = 0$ (upper row), $G = 132$ (middle row) and $G = 0.21$ (lower row).	92
6.3	Axial component of the optical force related to the heat dissipated by the nanoparticle as we increase the gain pumped to the system, (a) and (b), and the power of the laser, (c) and (d).	93

Chapter 1

Introduction

1.1 Plasmonics

Plasmonics is the study of interactions between free electrons in metals and electromagnetic fields at the nanoscale [23]. This phenomenon has been harnessed by humanity for centuries, predating the development of classical electromagnetic theory [7], which provided a foundational understanding of its mechanisms.

However, it was only in the last century that it gained prominence as an emerging field of research. This transformation was driven by the development of various new nano-technological methods [7], allowing for the synthesis of custom nanoparticles with nano-scale precision.

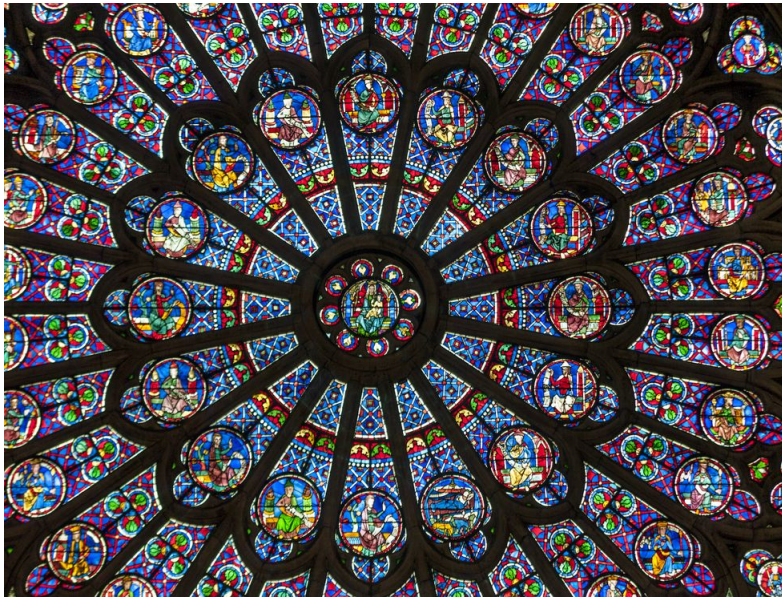


Figure 1.1: Notre Dame Cathedral: stained-glass rose window

The capability to unveil the physical phenomena underlying its operation, coupled with the ability to design and actualize desired nanostructures, has in fact expanded the scope of plasmonics. Originally confined to the realization of vibrant colors, it now finds applications across a broad spectrum, including areas such as bio-sensing, photovoltaics, plasmon-enhanced spectroscopy, and cancer therapy [5]. Most of these applications hinge on the plasmon's unique capacity to confine a considerable light intensity at sizes much smaller than the wavelength.

In the realm of plasmonics, three interrelated yet distinct phenomena can be discussed: the 3D oscillation of electron density, recognized as bulk plasmons (BPs); the 2D propagation of surface plasmon polaritons (SPPs) across surfaces or along waveguides; and the electron oscillations occurring in illuminated metal nanoparticles, termed localized surface plasmons (LSPs) [16]. This project will specifically

leverage the latter phenomenon.

While a metal nanoparticle can independently support LSPs regardless of its geometry, we will concentrate on spherical nanoparticles due to their greater stability and the clearer, though rich, electromagnetic phenomenology associated with them.

1.1.1 Localized Surface Plasmon Resonance

When the plasmon resonance of a LSP is activated, a superficial electron density begins to oscillate through the skin of the particle creating a local field, manifesting a resonance in frequency. This means that all the electromagnetic phenomena produced in these structures are extremely dependent on the spectral region in which they are studied. In principle, the center frequency of the Localized Surface Plasmon Resonance (LSPR) can appear in a wide spectral range between the deep violet and the near infrared. This location in the spectrum depends on some geometrical parameters such as the shape and the size of the nanoparticle and it is influenced as well by the environment of the nanoparticle (e. g. the index of refraction of the solvent hosting the nanoparticles).

To generate Localized Surface Plasmon Resonance (LSPR) within the visible spectrum, the most suitable plasmonic metals are silver and gold, with no absolute winner between the two due to their distinct advantages and drawbacks.

Silver, renowned for its low ohmic losses, emerges as a preferable choice for creating plasmonic emitters [4]. On the other hand, the natural biocompatibility of gold

and its ease of functionalization with various molecules make nanoparticles made of the latter more suitable for biological applications, such as bio-labeling and medical therapy. Both metals demonstrate resilience against photo-damage and maintain robustness in terms of optical, chemical, and thermal stability. Notably, gold nanoparticles exhibit higher absorption capabilities, making them more ideal for photothermal therapies [16].

1.2 Thermo-plasmonics

Recent years have seen a growing interest in using metal nanostructures to control temperature at the nanoscale. Metal nanoparticles are an ideal nano-source of heat, since when illuminated at its plasmonic resonance feature enhanced light absorption. This process allows for remote control of temperature using light, establishing the robust and adaptable photothermal mechanism that is the foundation of thermo-plasmonics [6].

1.2.1 Plasmonic Photothermal Therapy

Plasmonic photothermal therapy (PPTT) is a therapeutic approach where gold nanoparticles are introduced into cancerous cells through intravenous or intratumoral injection. Subsequently, these cells are exposed to near-infrared light, generating heat. This minimally invasive therapeutic strategy helps to mitigate the risk of severe infection-related complications often associated with surgery and bypasses the side

effects caused by the use of toxic drugs in chemotherapy. This method has the potential to serve as a promising alternative to conventional treatments like chemotherapy, radiotherapy, and surgery, particularly for localized tumors.

Preclinical investigations have demonstrated the considerable safety and effectiveness of PPTT in addressing xenograft tumors in mice. In 2021, AuroLase therapy, leveraging the photothermal effect of silica-gold nano-shells, underwent human clinical trials with encouraging results (ClinicalTrials.gov Identifiers: NCT02580535). Furthermore, gold nanorods have been employed in the treatment of spontaneously developing tumors in both canine and feline patients. Cancer is a prevalent cause of death in both cats and dogs, making this research directly relevant for veterinary applications. Additionally, both species exhibit comparable forms of cancer, resembling human cancer manifestations such as mammary gland tumors, which underscores the importance of this line of research for humans as well.

For the aforementioned reasons, several studies have investigated the treatment of spontaneous mammary gland tumors in cats and dogs [2] [29] [19] [3] [1]. The approach involved injecting gold nanorods directly into the solid tumors, followed by near-infrared (NIR) irradiation. Posterior to three treatment sessions, all cases showed significant tumor regression, with no instances of recurrence or metastasis. Importantly, there were no observed toxic effects on the blood profile, and liver and kidney functioning did not decrease after the treatment.

To summarize the advantages of Photothermal therapy, it is worth emphasizing that it circumvents the systemic side effects linked to conventional cancer treatments like chemotherapy. By focusing predominantly on localized solid tumors, PPTT

has the capacity to specifically target them, thus minimizing harm to surrounding healthy tissues. Additionally, because this method is a physical treatment and does not rely on specific drugs, it is not limited to specific tumor types. This means that PPTT has the potential to serve as a “universal” treatment for a wide range of cancer types, overcoming issues related to drug resistance that often arise over time with other therapies.

Moreover, recent advancements in the field underscore the promising potential of PPTT not only in treating existing tumors but also in effectively preventing the recurrence and spread of metastasis [22]. This encouraging development opens new avenues for research and application, suggesting that PPTT could play a pivotal role in addressing the challenges associated with metastatic cancer, a key aspect in advancing cancer therapeutics.

1.2.2 Optical trap efficiency

In an optical tweezer, the pressure exerted by radiation is a consequence of momentum conservation during the absorption and scattering of photons. In addition to the scattering force, electromagnetic fields induce polarization in dielectric materials, resulting in a gradient force pointing towards high-intensity field regions. This gradient force, originating from a single tightly focused laser beam, enables the trapping of individual nano or micro-sized dielectric particles in three dimensions, giving rise to what is now known as optical tweezers. This technique has found widespread applications in biology, physics, chemistry, and materials science, offering the ability to apply well-defined forces and torques while non-invasively manipulating nano

and microscale objects.

Optical tweezers designed for dielectric particles, primarily rely on the gradient force. However, metallic nanoparticles strongly absorb and scatter light near their localized surface plasmon resonance (LSPR), which increases the contribution of the scattering force and complicates stable trapping. Nevertheless, Svoboda and Block demonstrated in 1994 that metallic nanoparticles can be stably trapped with sufficiently off-resonant optical tweezers (using a focused laser with a wavelength not too close to the LSPR of the trapped particle). These properties include electrical field enhancement, increased fluorescence and Raman scattering, as well as local heating. The delicate balance between gradient and scattering force near the LSPR allows for precise manipulation of trapped particles. This combination of precise spatial control and plasmonic properties makes optical trapping and manipulation of plasmonic particles crucial for a wide range of research fields, both fundamental and applied.

The absorption of radiation leads to heat generation through non-radiative decay channels, involving electron–electron and electron–phonon interactions. Plasmonic nanoparticles, known for their efficient nanoscale heating, are being increasingly applied in cancer treatment. Due to their small volume, bubble formation is suppressed, and local temperatures significantly exceeding the boiling point of the surrounding medium can be achieved. Even under off-resonant excitation conditions, as present in an optical trap, considerable temperature increases can be observed.

Lastly, particle temperature can affect trap stability. Ohlinger et al. showed that successive trapping of silver nanoparticles destabilized the trap if the red-shifted cou-

pled plasmon resonance was close enough to the trapping laser wavelength. This was attributed to two effects: firstly, the coupled plasmon resonance being closer to the trapping laser wavelength shifts the force balance between gradient and scattering force towards the scattering contribution; secondly, this also leads to more efficient plasmonic heating. Both effects contribute to trap destabilization and particle release [30] [33].

Chapter 2

Choosing the right nanoparticle

While still keeping our analysis in the realm of spherically symmetric nanoparticles, one can study more complicated configurations, such as coated spheres

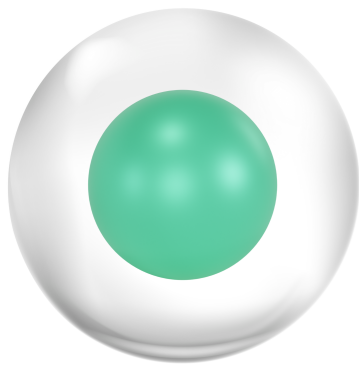


Figure 2.1: Coated sphere.

depending on the ordering of the used materials in these structures, one can have core-shell and nano-shell particles. The first configuration is when an internal metal core is coated by a dielectric shell, while the second one is when an internal dielectric core is coated with metal. In this thesis, we will work on the latter configuration for a number of reasons, including the ability to modulate

the resonance frequency by varying the shell thickness (i. e., the ratio between the

internal and the external radius) [9] and the fact that, in this configuration, it is easy to include additional active species in the core of the nanoparticle, such as gain elements (e.g., quantum dots, fluorescent dyes, etc.). Those active elements, when pumped by an external source, can act as amplifiers for the electromagnetic fields at a specific range of frequencies.

This allows the interplay between the quantum emission of the gain elements to be maximized by overlapping their emission center frequency with the plasmon resonance frequency. This coupling adds an additional dimension to the parameter space of the problem, resulting in intense changes in the electromagnetic fields around the structure, including extreme amplification and emissive regimes where the resonant plasmonic field can be summoned by a non-resonant pump.

The result is a further, exponential increase in the already large variety of applications, allowing for targeted photothermal therapy, enhanced spectroscopy, and spasing [26] [31] [32].

2.1 Gain enhanced nano-shell

2.1.1 The Gain assisted Medium

A gain medium can be modeled as a two-level system through the Optical Bloch equations in the density matrix formalism. This is achieved by introducing a phenomenological pump instead of the typical thermal bath used to model absorbing

elements:

$$\frac{d\rho_{12}}{dt} - \left(i\omega_{12} - \frac{1}{\tau_2} \right) \rho_{12} = \frac{iN\boldsymbol{\mu} \cdot \tilde{\mathbf{E}}_h}{\hbar} \quad (2.1)$$

$$\frac{dN}{dt} + \frac{N - \tilde{N}}{\tau_1} = \frac{2i(\rho_{12} - \rho_{21})\boldsymbol{\mu} \cdot \tilde{\mathbf{E}}_h}{\hbar}. \quad (2.2)$$

Here, the electric field of the gain medium, $\tilde{\mathbf{E}}_h$, interacts with a single gain element of dipole moment $\boldsymbol{\mu}$. Also, ρ_{ij} is the i, j element of the density matrix. The constants describing phase and energy relaxation processes due to interaction with the thermal bath are τ_1 , $\tilde{\tau}_1$ and τ_2 . Where

$$\tau_1 = \frac{\tilde{\tau}_1}{W\tilde{\tau}_1 + 1},$$

is the typical energy relaxation time. And

$$\tau_2 = \frac{2}{\Delta} \quad (2.3)$$

correspond to the typical relaxation time of the phase.

The transition frequency between levels 1 and 2 is

$$\omega_{12} = \frac{E_2 - E_1}{\hbar},$$

$N = \rho_{22} - \rho_{11}$ is the population inversion, and the corresponding value of N for the thermal equilibrium of the reservoir is given by

$$\tilde{N} = \frac{W\tau_1 - 1}{W\tau_1 + 1}, \quad (2.4)$$

where W is the phenomenological pump rate.

The presence of \tilde{N} as defined in Eq. 2.4 in Equation 2.2 means that, when the right-hand term of the same equation is negligible, the population inversion is driven to \tilde{N} in a time of the order of τ_1 . By choosing $\tilde{N} > 0$ here, we are effectively modeling a pump that drives the active elements to its excited state.

In this framework, the polarization of the gain medium, arising from the collective behavior of the gain elements' population, can be calculated as:

$$\tilde{\mathbf{P}}_h = \varepsilon_0 \chi_b \tilde{\mathbf{E}}_h + \frac{n}{4\pi} \int_{\Omega} \rho_{12} \boldsymbol{\mu} d\Omega \quad (2.5)$$

where χ_b is the susceptibility of the dielectric host in which the gain elements are dispersed. The right side of Expression 2.5 accounts for the contribution of a population of gain elements with particle density n , assuming a random distribution for the dipole moments $\boldsymbol{\mu}$ which are activated by the element of the density matrix ρ_{12} , accounting for the probability of transition. This effect is then averaged over the solid angle. Expression 2.5 shows that if the probability of transition were independent of the field in the gain region, the right term would just be averaged out. However, Equation 2.1 has a driving term on the right-hand side that favors the transition of the gain elements whose dipole moment is parallel to the electric field $\tilde{\mathbf{E}}_h$.

If we now define the active contribution to the polarization $\tilde{\mathbf{\Pi}}_h$ as:

$$\tilde{\mathbf{\Pi}}_h = \frac{n}{4\pi} \int_{\Omega} \rho_{12} \boldsymbol{\mu} d\Omega, \quad (2.6)$$

Expression 2.5 can be rewritten as:

$$\tilde{\mathbf{P}}_h = \varepsilon_0 \chi_b \tilde{\mathbf{E}}_h + \tilde{\mathbf{\Pi}}_h. \quad (2.7)$$

Also, considering that it is possible to demonstrate that

$$\int_{\Omega} (\boldsymbol{\mu} \cdot \tilde{\mathbf{E}}_h) \boldsymbol{\mu} d\Omega = \frac{4\pi}{3} \mu^2 \tilde{\mathbf{E}}_h,$$

one can rewrite the system of equations 2.1-2.2 in terms of the time evolution of the dynamic part of the polarization in the gain medium:

$$\frac{d\tilde{\mathbf{\Pi}}_h}{dt} - \left(i\omega_{21} - \frac{1}{\tau_2} \right) \tilde{\mathbf{\Pi}}_h = \frac{in\mu^2 N}{3\hbar} \tilde{\mathbf{E}}_h, \quad (2.8)$$

$$\frac{dN}{dt} + \frac{N - \tilde{N}}{\tau_1} = \frac{2i}{n\hbar} (\tilde{\mathbf{\Pi}}_h - \tilde{\mathbf{\Pi}}_h^*) \cdot \tilde{\mathbf{E}}_h. \quad (2.9)$$

Now, applying the rotating wave approximation

$$\begin{aligned} \tilde{\mathbf{E}}_h(t) &= \frac{1}{2} [\mathbf{E}_h(t)e^{-i\omega t} + \mathbf{E}_h^*(t)e^{i\omega t}], \\ \tilde{\mathbf{\Pi}}_h(t) &= \frac{1}{2} \mathbf{\Pi}_h(t)e^{i\omega t}, \\ \tilde{\mathbf{P}}_h(t) &= \frac{1}{2} [\mathbf{P}_h(t)e^{-i\omega t} + \mathbf{P}_h^*(t)e^{i\omega t}], \end{aligned}$$

where $\mathbf{E}_h(t)$, $\mathbf{\Pi}_h(t)$ and $\mathbf{P}_h(t)$ represent slow dependency on time.

When averaged on fast variations in time, (2.8) and (2.9) becomes:

$$\frac{d\mathbf{\Pi}_h}{dt} - \left[i(\omega - \omega_{21}) - \frac{1}{\tau_2} \right] \mathbf{\Pi}_h = \frac{in\mu^2 N}{6\hbar} \mathbf{E}_h, \quad (2.10)$$

$$\frac{dN}{dt} + \frac{N - \tilde{N}}{\tau_1} = \frac{i}{n\hbar}(\mathbf{E}_h \cdot \mathbf{\Pi}_h - \mathbf{E}_h^* \cdot \mathbf{\Pi}_h^*). \quad (2.11)$$

Finally, noticing that the steady state permittivity can be written as:

$$\varepsilon_h(\omega) = \varepsilon_b - \frac{G\Delta}{2(\omega - \omega_{21} + i\Delta)}, \quad (2.12)$$

where the parameter

$$G = -\frac{n\mu^2\tau_2}{3\hbar\varepsilon_0}\tilde{N}, \quad (2.13)$$

gives an absolute measure of the gain quantity used in the system, one can rewrite the system of equations 2.10-2.11 as:

$$\frac{d\mathbf{\Pi}_h}{dt} - \left[i(\omega - \omega_{21}) - \frac{1}{\tau_2} \right] \mathbf{\Pi}_h = -\frac{i\varepsilon_0 G N}{\tau_2 \tilde{N}} \mathbf{E}_h, \quad (2.14)$$

$$\frac{dN}{dt} + \frac{N - \tilde{N}}{\tau_1} = -\frac{i}{2n\hbar}(\mathbf{\Pi}_h \cdot \mathbf{E}_h^* - \mathbf{\Pi}_h^* \cdot \mathbf{E}_h), \quad (2.15)$$

This new version of the system of equations allows us to explore the time evolution in the gain-rich medium for different amounts of the gain quantity G . One can easily see here that if $G = 0$ (no gain is used in the system) or when $\tilde{N} = 0$ (there are gain elements but they are not externally pumped), the dynamic part of the polarization $\mathbf{\Pi}_0$ remains null, and the polarization in this region reverts to the passive one (see Expression 2.7).

2.1.2 The Metal

To describe the time evolution of the polarization in the metal region of the nanoparticle, produced by the electric field \mathbf{E}_m (i. e., the electric field in the metal region), we use the Drude's free electron model:

$$\frac{d^2\mathbf{r}}{dt^2} + 2\gamma\frac{d\mathbf{r}}{dt} = \frac{e}{m_e}\tilde{\mathbf{E}}_m \quad (2.16)$$

where \mathbf{r} is the displacement of the electron cloud with respect to the equilibrium position, m_e and e are the electron mass and charge respectively, and γ is the ionic collisions friction coefficient. This charge dislocation produces a polarization along $\hat{\mathbf{r}}$, which one can calculate as:

$$\tilde{\mathbf{\Pi}}_m = n_e e \mathbf{r}, \quad (2.17)$$

where n_e is the electron density in the metal. Substituting (2.17) into (2.16), and considering that the plasma frequency is given by

$$\omega_{pl}^2 = \frac{n_e e^2}{\varepsilon_0 m_e},$$

we can finally obtain the equation for the time evolution of $\tilde{\mathbf{\Pi}}_m$:

$$\frac{d^2\tilde{\mathbf{\Pi}}_m}{dt^2} + 2\gamma\frac{d\tilde{\mathbf{\Pi}}_m}{dt} = \varepsilon_0\omega_{pl}^2\tilde{\mathbf{E}}_m. \quad (2.18)$$

It is important to mention that $\tilde{\mathbf{\Pi}}_m$ represents the dynamic part of the polarization in the metal due to the electrons' displacement. However, to be able to describe a more realistic electromagnetic response for this material, one has to take into account the

passive contribution due to the ionic lattice as well. The resulting polarization in the metal will therefore be:

$$\tilde{\mathbf{P}}_m = \varepsilon_0 \chi_\infty \tilde{\mathbf{E}}_m + \tilde{\mathbf{\Pi}}_m. \quad (2.19)$$

We will now use the rotating wave approximation, as we did in the previous section for the gain medium. This means that the electric field and polarizations can be written in the form:

$$\tilde{\mathbf{E}}_m(t) = \frac{1}{2} [\mathbf{E}_m(t)e^{-i\omega t} + \mathbf{E}_m^*(t)e^{i\omega t}] \quad (2.20)$$

$$\mathbf{\Pi}_m(t) = \frac{1}{2} [\mathbf{\Pi}_m(t)e^{-i\omega t} + \mathbf{\Pi}_m^*(t)e^{i\omega t}] \quad (2.21)$$

$$\tilde{\mathbf{P}}_m(t) = \frac{1}{2} [\mathbf{P}_m(t)e^{-i\omega t} + \mathbf{P}_m^*(t)e^{i\omega t}] \quad (2.22)$$

where $\mathbf{E}_m(t)$, $\mathbf{\Pi}_m(t)$, and $\mathbf{P}_m(t)$ represent a slow dependency on time.

If we now substitute expressions 2.20-2.22 into equation 2.18 and average on fast time variations, we can finally obtain the time evolution equation for the dynamic part of the polarization in the metal region:

$$\frac{d\mathbf{\Pi}_m}{dt} - \frac{\omega^2 + 2i\gamma\omega}{2(\gamma - i\omega)} \mathbf{\Pi}_m = \frac{\varepsilon_0 \omega_{pl}^2}{2(\gamma - i\omega)} \mathbf{E}_m. \quad (2.23)$$

It might be worth noting that the steady-state solution of equation 2.23 allows us to obtain the steady-state Drude permittivity in its classical form:

$$\varepsilon_m(\omega) = \varepsilon_\infty - \frac{\omega_{pl}^2}{\omega(\omega + 2i\gamma)}. \quad (2.24)$$

Accounting for the Interband Transitions Losses

The expression 2.24 for Drude permittivity tends to underestimate losses arising from interband transitions. This becomes crucial for some applications, as an example, when assessing heat generation in a nanoparticle. To address these additional losses, we calculate a frequency-dependent $\varepsilon_\infty(\omega)$ using the following expression:

$$\varepsilon_\infty(\omega) = \varepsilon_m^{JC}(\omega) + \frac{\omega_{pl}^2}{\omega(\omega + 2i\gamma)} \quad (2.25)$$

Here, $\varepsilon_m(\omega)$ is the dielectric permittivity of the metal, determined by interpolation from the Johnson and Christy's experimental data set [15] (however, it can be generalized to any experimental data set). The resulting $\varepsilon_\infty(\omega)$ is then used instead of the static ε_∞ in the Drude model formula (2.24). The resulting metal permittivity

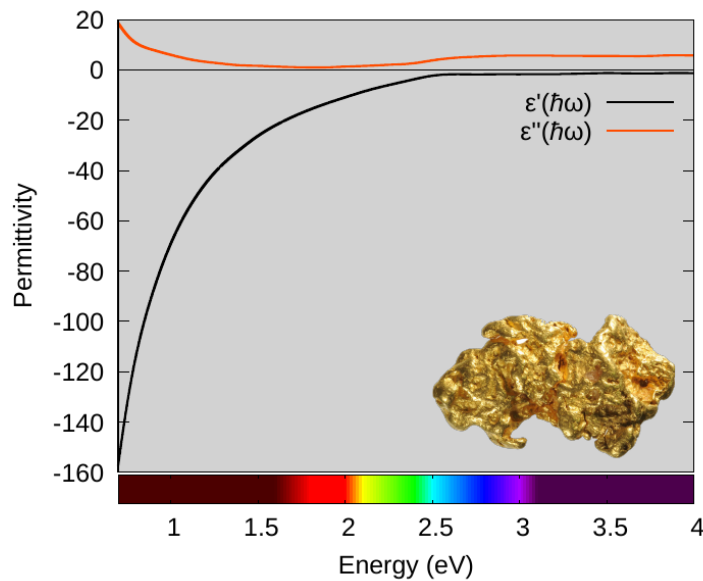


Figure 2.2: Complex permittivity for gold, calculated using a free electron model and including additional losses through the interpolation of the data measured by Johnson and Christy.

for gold is presented in Figure 2.2, where we presented the frequency dependence in terms of energy per photon $\hbar\omega$ and presented in electronvolts.

2.1.3 The Solvent

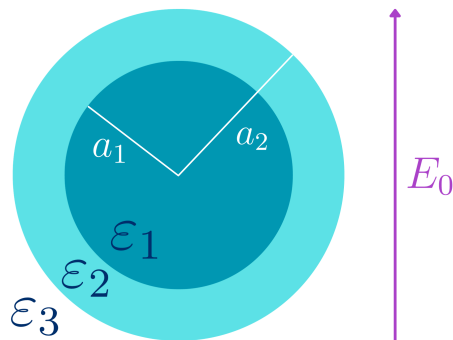
Finally, it is important to mention that the nanoparticle is hosted in a passive solvent, so the remaining component in the system is a simple dielectric, characterized by a real constant and a linear electromagnetic response. If, for example, the nanoparticle is dissolved in water, one has simply to consider $\varepsilon_W = 1.7689$ for the third permittivity.

This complete the discussion on the constitutive model of the materials in play, consequently, attention can now shift to the effects arising from nanoparticle geometry. Due to the interface nature of the plasmons, these effects are as significant as the material composition of the nanostructure. In the subsequent chapter, it will be demonstrated that these shape effects can be effectively modeled as the boundary conditions of a second-order partial differential equation problem.

Chapter 3

Electromagnetic model

3.1 The coated sphere



The nanoparticle in focus consists of a nucleus with a radius of a_1 and an electric permittivity of ϵ_1 , which is enveloped by a shell with an external radius of a_2 and an electric permittivity of ϵ_2 , the whole structure is surrounded by a solvent with an electric permittivity of ϵ_3 (see Figure 3.1).

Figure 3.1: A sphere of permittivity ϵ_1 , in a shell of permittivity ϵ_2 in a host of permittivity ϵ_3 .

The system is subjected to an optical electric field \mathbf{E}_0 , assumed to be a plane

wave. To simplify calculations, we position the geometrical center of the nanoparticle at the origin of the coordinate system.

3.2 Quasistatic Approximation

When the size of a nanoparticle is small compared to the wavelength λ of the incident field (i. e., $\lambda \gg a_2$), we can apply the quasistatic approximation [31, 32, 9]. In this regime, the exciting electric field can be considered uniform in the region of interest.

In our calculations, we consider the exciting field as a plane wave propagating alongside the x -axis with polarization in the z -direction. In the quasi-static approximation, the propagating part of the plane wave, e^{kx} (where k is the wave-number), tends to 1 as $\lambda \rightarrow \infty$ (i. e., $k \rightarrow 0$). Consequently, we express the incident electric field as:

$$\mathbf{E}_i = E_0 \hat{\mathbf{k}} e^{-i\omega t}, \quad (3.1)$$

where E_0 is the amplitude of the electric field, $\hat{\mathbf{k}}$ is the unit vector of the z -axis defining the polarization of the wave, and ω is the angular frequency. The corresponding magnetic field, $\mathbf{H}_i(t)$, is negligible in this approximation. By continuity at the boundary, this condition extends inside the nanoparticle, resulting in $\mathbf{H}(\mathbf{r}, t) \sim 0$ everywhere. Consequently, the magnetic induction field $\mathbf{B}(\mathbf{r}, t)$ is also negligible, leading to the following expression:

$$\nabla \times \mathbf{E}(\mathbf{r}, t) = 0. \quad (3.2)$$

Equation 3.2 implies that it should exist a scalar function $\Phi(\mathbf{r}, t)$ such that:

$$\mathbf{E}(\mathbf{r}, t) = -\nabla\Phi(\mathbf{r}, t). \quad (3.3)$$

If we now consider the Maxwell equation for the Gauss' law in a material

$$\nabla \cdot \mathbf{D}(\mathbf{r}, t) = 0, \quad (3.4)$$

where $\mathbf{D}(\mathbf{r}, t)$ is the displacement vector which is related to the electric field through $\mathbf{D}(\mathbf{r}, t) = \varepsilon_0\varepsilon(\mathbf{r}, \omega)\mathbf{E}(\mathbf{r}, t)$, where $\varepsilon(\mathbf{r}, \omega)$ is the relative dielectric permittivity of the material. Therefore,

$$\nabla \cdot \mathbf{D}(\mathbf{r}, t) = \varepsilon_0\varepsilon(\mathbf{r}, \omega)\nabla \cdot \mathbf{E}(\mathbf{r}, t) + \varepsilon_0\nabla\varepsilon(\mathbf{r}, \omega) \cdot \mathbf{E}(\mathbf{r}, t) = 0.$$

which gives the following expression for the divergence of the electric field:

$$\nabla \cdot \mathbf{E}(\mathbf{r}, t) = \left[\frac{\nabla\varepsilon(\mathbf{r}, \omega)}{\varepsilon(\mathbf{r}, \omega)} \right] \cdot \mathbf{E}(\mathbf{r}, t). \quad (3.5)$$

If we can consider all of the materials we model as homogeneous mediums, we have $\varepsilon(\mathbf{r}, \omega) = \varepsilon(\omega)$, which means

$$\frac{\nabla\varepsilon(\mathbf{r}, \omega)}{\varepsilon(\mathbf{r}, \omega)} \sim 0. \quad (3.6)$$

and therefore, (3.5) becomes

$$\nabla \cdot \mathbf{E}(\mathbf{r}, t) = 0. \quad (3.7)$$

This means that, providing that condition 3.6 is satisfied, one can substitute (3.3) in

(3.7), obtaining the Laplace equation for $\Phi(\mathbf{r}, t)$

$$\nabla^2 \Phi(\mathbf{r}, t) = 0, \quad (3.8)$$

whose general solution, in spherical coordinates, is given by

$$\Phi(\mathbf{r}, t) = \sum_0^{\infty} \left[A_l r^l + \frac{B_l}{r^{l+1}} \right] P_l(\cos \theta), \quad (3.9)$$

where $P_l(\cos \theta)$ are the Legendre polynomials and θ is the polar angle in spherical coordinates.

The solution (3.9) should be applicable in three regions: the nucleus (i. e., region 1), the shell (i. e., region 2), and outside the nanoparticle (i. e., region 3) (see Figure 3.1).

In region 1, which includes $r = 0$, to avoid singularities, it is necessary to set $B_l^{(1)} = 0$ for all l . In region 3, as $r \rightarrow \infty$, the field must connect with the incident field $\mathbf{E}_i(t)$ given by (3.1). This corresponds to the potential:

$$\Phi_{\infty}(t) = -E_0 z e^{-i\omega t} = -E_0 r \cos \theta e^{-i\omega t} = -E_0 r^1 P_1(\cos \theta) e^{-i\omega t}. \quad (3.10)$$

To achieve this connection and ensure

$$\lim_{r \rightarrow \infty} \Phi_3(\mathbf{r}, t) = \Phi_{\infty}(t),$$

it is necessary to set $A_1^{(2)} = -E_0 e^{-i\omega t}$ and $A_l^{(2)} = 0$ for all $l \neq 1$.

Hence, the potential in all of the space is given by the following equations

$$\Phi_1(\mathbf{r}, t) = \sum_{l=0}^{\infty} A_l^{(1)} r^l P_l(\cos \theta), \quad (3.11)$$

$$\Phi_2(\mathbf{r}, t) = \sum_{l=0}^{\infty} \left[A_l^{(2)} r^l + \frac{B_l^{(2)}}{r^{l+1}} \right] P_l(\cos \theta), \quad (3.12)$$

$$\Phi_3(\mathbf{r}, t) = \sum_{l=0}^{\infty} \left[-\delta_{l1} E_0 e^{-i\omega t} r^l + \frac{B_l^{(3)}}{r^{l+1}} \right] P_l(\cos \theta). \quad (3.13)$$

The constants $A_l^{(1)}$, $A_l^{(2)}$, $B_l^{(2)}$ and $B_l^{(3)}$ can be found by applying the radial continuity boundary conditions

$$\Phi_1(a_1 \hat{\mathbf{r}}(\theta, \varphi), t) = \Phi_2(a_1 \hat{\mathbf{r}}(\theta, \varphi), t), \quad (3.14)$$

$$\Phi_2(a_2 \hat{\mathbf{r}}(\theta, \varphi), t) = \Phi_3(a_2 \hat{\mathbf{r}}(\theta, \varphi), t); \quad (3.15)$$

and the tangential continuity boundary conditions

$$\varepsilon_1 E_1^r a_1 \hat{\mathbf{r}}(\theta, \varphi), t) = \varepsilon_2 E_2^r a_1 \hat{\mathbf{r}}(\theta, \varphi), t), \quad (3.16)$$

$$\varepsilon_2 E_2^r a_2 \hat{\mathbf{r}}(\theta, \varphi), t) = \varepsilon_3 E_3^r a_2 \hat{\mathbf{r}}(\theta, \varphi), t). \quad (3.17)$$

Finally, by propagating the Kronecker delta $\delta_{1\ell}$ we obtain

$$A_1^{(1)} = \frac{B_1^{(2)}}{a_1^3} + A_1^{(2)} \quad (3.18)$$

$$A_1^{(2)} = \frac{B_1^{(3)} - B_1^{(2)}}{a_2^3} - E_0, \quad (3.19)$$

$$B_1^{(2)} = \frac{a_1^3(\varepsilon_1 - \varepsilon_2)E_0 - \rho^3(\varepsilon_1 - \varepsilon_2)B_1^{(3)}}{\varepsilon_1 - \rho^3(\varepsilon_1 - \varepsilon_2) + 2\varepsilon_2}, \quad (3.20)$$

$$B_1^{(3)} = a_2^3 \frac{(\varepsilon_2 - \varepsilon_3)(\varepsilon_1 + 2\varepsilon_2) + \rho^3(\varepsilon_1 - \varepsilon_2)(\varepsilon_3 + 2\varepsilon_2)}{(\varepsilon_2 + 2\varepsilon_3)(\varepsilon_1 + 2\varepsilon_2) + 2\rho^3(\varepsilon_2 - \varepsilon_3)(\varepsilon_1 - \varepsilon_2)} E_0, \quad (3.21)$$

where we also introduced the ratio between radius $\rho = \frac{a_1}{a_2}$.

We will now utilize the obtained results to determine the polarizability, denoted as α , of the nanoparticle. This physical property is connected to all the optical characteristics of a nano-object and is defined as the complex constant relating the dipole moment of the nanoparticle to the incident field:

$$\mathbf{p} = \alpha(\omega)\mathbf{E}_0. \quad (3.22)$$

Here, the frequency dependence of $\alpha(\omega)$ is inherited from the frequency-dependent permittivities of the metal and gain medium. It's also important to note that the dipole moment \mathbf{p} is associated with the external region (region 3).

The potential of a dipolar field can be written as:

$$\Phi_{\text{dip}}(r, \theta) = \frac{\hat{\mathbf{r}} \cdot \mathbf{p}}{4\pi\varepsilon r^2} = \frac{p \cos(\theta)}{4\pi\varepsilon r^2}, \quad (3.23)$$

comparing it with the expression for $\Phi_3(\mathbf{r}, t)$, two terms can be identified:

$$\frac{B_1^{(3)} \cos(\theta)}{r^2} = \frac{p \cos(\theta)}{4\pi\epsilon_3 r^2}. \quad (3.24)$$

If we now solve equation 3.24 for p , and given that $\alpha = \frac{p}{E}$, we obtain:

$$\alpha = \frac{B_1^{(3)}(4\pi\epsilon_3)}{E_0}, \quad (3.25)$$

which, using expression 3.21 for $B_1^{(3)}$ finally gives:

$$\alpha = 4\pi\epsilon_3 a_2^3 \frac{(\epsilon_2 - \epsilon_3)(\epsilon_1 + 2\epsilon_2) + \rho^3(\epsilon_1 - \epsilon_2)(\epsilon_3 + 2\epsilon_2)}{(\epsilon_2 + 2\epsilon_3)(\epsilon_1 + 2\epsilon_2) + 2\rho^3(\epsilon_2 - \epsilon_3)(\epsilon_1 - \epsilon_2)} \quad (3.26)$$

It is worth mentioning here that this also means that the scattered field of a coated sphere in the quasistatic approximation is equivalent to an ideal dipolar field of dipolar moment $\alpha\mathbf{E}_0$.

3.2.1 Cross Sections

From an optical perspective, the intriguing feature of a frequency-dependent polarization $\alpha(\omega)$, showcasing a resonant maximum at a specific frequency ω_{sp} , lies in its ability to significantly enhance the efficiency of light scattering and absorption by a metal nanoparticle around that resonant frequency [20].

This enhancement is attributed to the close relationship between the polarizability and the corresponding cross sections for scattering, absorption, and extinction.

These cross sections can be calculated using the Pointing vector, as outlined in [8]. The resulting scattering cross section, quantifying the amount of dispersed light, is

$$C_{sca} = \frac{k^4}{6\pi} |\alpha|^2, \quad (3.27)$$

while the absorption cross section, quantifying the amount of luminous energy absorbed by the nanoparticle, is

$$C_{abs} = k \operatorname{Im}\{\alpha\} - \frac{k^4}{6\pi} |\alpha|^2, \quad (3.28)$$

and the extinction cross section (the sum of the previous two), quantifying the amount of radiation extinguished by the nanoparticle, is

$$C_{ext} = k \operatorname{Im}\{\alpha\}. \quad (3.29)$$

Equation (3.29) holds true when scattering is significantly smaller than absorption.

Absorption tends to be more pronounced than scattering in the case of small particles. This phenomenon is exemplified by the alteration of white light as it traverses a collection of minute particles, leading to a reddish hue. A simple demonstration involves introducing a few drops of milk into a container of clear water: a focused beam of white light exhibits a reddish tint upon passing through this suspension. This color change occurs because shorter-wavelength blue light is more effectively absorbed than longer-wavelength red light. The heightened extinction with decreasing wavelengths is a general attribute of nonabsorbing particles that are small compared to the wavelength of light. Familiar instances of such effects include the captivating

red and orange tones observed in sunset skies, influenced in part by molecular scattering. Small particles have the capacity to intensify the reddish appearance during sunset [8].

3.3 Mie Theory

When the size of a spherical nanoparticle is comparable to the wavelength of the incident field, the approximation $\lambda \gg a_2$ is no longer applicable. In this scenario, the spatial dependency of the incident field, governed by the propagation of the wave, becomes significant, and the quasistatic approximation breaks down. To describe scattering in this regime, we employ Mie theory, formulated by Gustav Mie in 1908. This approach offers a robust and mathematically rigorous framework for describing the scattering and absorption of light by spherical particles. Mie theory facilitates a comprehensive analysis of the interaction between electromagnetic waves and nanoparticles, considering various parameters such as particle size, refractive index, and wavelength.

In this section, we adopt the formalism presented in [8] as a reference for Mie theory. Additionally, all subsequent calculations are performed in the optical approximation, (i. e., $\mu_r = 1$), and assume a sufficiently homogeneous material, ensuring that condition 3.6 is still satisfied.

Utilizing the time-oscillating solutions of the wave equation for the electromag-

netic field

$$\tilde{\mathbf{E}}(\mathbf{r}, t) = \frac{1}{2} [\mathbf{E}(\mathbf{r})e^{-i\omega t} + \mathbf{E}(\mathbf{r})e^{i\omega t}], \quad (3.30)$$

$$\tilde{\mathbf{H}}(\mathbf{r}, t) = \frac{1}{2} [\mathbf{H}(\mathbf{r})e^{-i\omega t} + \mathbf{H}(\mathbf{r})e^{i\omega t}]; \quad (3.31)$$

the spatial dependence of the complex envelopes $\mathbf{E}(\mathbf{r})$ and $\mathbf{H}(\mathbf{r})$ is determined by the Helmholtz equations

$$\nabla^2 \mathbf{E}(\mathbf{r}) - \frac{\omega^2}{c^2} \varepsilon(\omega) \mathbf{E}(\mathbf{r}) = 0, \quad (3.32)$$

$$\nabla^2 \mathbf{H}(\mathbf{r}) - \frac{\omega^2}{c^2} \varepsilon(\omega) \mathbf{H}(\mathbf{r}) = 0. \quad (3.33)$$

Taking into account the dispersion relation $k = \frac{\omega^2}{c^2} \varepsilon(\omega)$, these can be rearranged as

$$\nabla^2 \mathbf{E} + k^2 \mathbf{E} = 0, \quad (3.34)$$

$$\nabla^2 \mathbf{H} + k^2 \mathbf{H} = 0. \quad (3.35)$$

We also observe that employing expressions 3.30 and 3.31 for $\tilde{\mathbf{E}}$ and $\tilde{\mathbf{H}}$ reduces the relevant Maxwell's equations to:

$$\nabla \times \mathbf{E} = i\omega\mu\mathbf{H}, \quad (3.36)$$

$$\nabla \times \mathbf{H} = -i\omega\varepsilon\mathbf{E}. \quad (3.37)$$

This implies that the vector functions forming the basis for projecting the solution of our scattering problem must simultaneously satisfy the systems of equations 3.34-3.35 and 3.36-3.37.

To construct this basis, we define the vector function $\mathbf{M}(\mathbf{r})$ using a scalar spatial function $\psi(\mathbf{r})$ (referred to as the generating function) and an arbitrary constant vector \mathbf{c} (defined as the guiding or pilot vector) as follows:

$$\mathbf{M}(\mathbf{r}) = \nabla \times [\mathbf{c}\psi(\mathbf{r})]. \quad (3.38)$$

Utilizing the differential properties of ∇ and a few vector identities, it can be demonstrated that $\mathbf{M}(\mathbf{r})$ satisfies the equation:

$$\nabla^2 \mathbf{M}(\mathbf{r}) + k^2 \mathbf{M}(\mathbf{r}) = \nabla \times \{\mathbf{c}[\nabla^2 \psi(\mathbf{r}) + k^2 \psi(\mathbf{r})]\}, \quad (3.39)$$

which means that $\mathbf{M}(\mathbf{r})$ satisfies the Helmholtz vector equation if $\psi(\mathbf{r})$ is a solution to the following scalar Helmholtz equation.

$$\nabla^2 \psi(\mathbf{r}) + k^2 \psi(\mathbf{r}) = 0. \quad (3.40)$$

consequently, by using a appropriate scalar function $\psi(\mathbf{r})$, the correspondent vector function will satisfy equations 3.34 and 3.35.

To complete our basis, we need a second function which will allow our solutions to satisfy equations 3.36 and 3.37. This means that the new function has to comply with a similar relation with $\mathbf{M}(\mathbf{r})$, so we construct it as:

$$\mathbf{N}(\mathbf{r}) = \nabla \times [\mathbf{d}\chi(\mathbf{r})]. \quad (3.41)$$

It is easy to show that $\mathbf{N}(\mathbf{r})$ also satisfies the vector Helmholtz equation:

$$\nabla^2 \mathbf{N}(\mathbf{r}) + k^2 \mathbf{N}(\mathbf{r}) = 0, \quad (3.42)$$

and has the property:

$$\nabla \times \mathbf{N}(\mathbf{r}) = k \mathbf{M}(\mathbf{r}). \quad (3.43)$$

In summary, $\mathbf{M}(\mathbf{r})$ and $\mathbf{N}(\mathbf{r})$ fulfill all the necessary properties to constitute a basis of vector functions for projecting the solutions of our electromagnetic problem, provided that the generating function $\psi(\mathbf{r})$ solves the scalar Helmholtz equation. The problem we are addressing exhibits spherical symmetry, requiring the generating function $\psi(\mathbf{r})$ to satisfy the Helmholtz equation in spherical coordinates:

$$\frac{1}{r^2} \frac{\partial}{\partial r} \left(r^2 \frac{\partial \psi}{\partial r} \right) + \frac{1}{r^2 \sin \theta} \frac{\partial}{\partial \theta} \left(\sin \theta \frac{\partial \psi}{\partial \theta} \right) + \frac{1}{r^2 \sin^2 \theta} \frac{\partial^2 \psi}{\partial \varphi^2} + k^2 \psi = 0, \quad (3.44)$$

Through the technique of separation of variables, wherein we seek a solution in the form $\psi(r, \theta, \varphi) = R(r)\Theta(\theta)\Phi(\varphi)$, we obtain the following set of separated equations:

$$\frac{d^2 \Phi}{d\varphi^2} + m^2 \Phi = 0, \quad (3.45)$$

$$\frac{1}{\sin \theta} \frac{d}{d\theta} \left(\sin \theta \frac{d\Theta}{d\theta} \right) + \left[n(n+1) - \frac{m^2}{\sin^2 \theta} \right] \Theta = 0, \quad (3.46)$$

$$\frac{d}{dr} \left(r^2 \frac{dR}{dr} \right) + [k^2 r^2 - n(n+1)] R = 0, \quad (3.47)$$

where the separation constants m and n are determined by the supplementary conditions that ψ must satisfy.

The linear independent solutions of (3.45) are

$$\Phi_e = \cos(m\varphi), \quad (3.48)$$

$$\Phi_o = \sin(m\varphi), \quad (3.49)$$

where e and o denote even and odd.

Also, we require ψ to be a single valued function of the azimuthal angle φ

$$\lim_{\nu \rightarrow 2\pi} \psi(\varphi + \nu) = \psi(\varphi), \quad (3.50)$$

for all φ except, possibly, at the points on the boundary between regions with different properties. However, we are only interested in solutions to the scalar Helmholtz equation at interior points of homogeneous regions. Therefore, (3.50) requires $m \in \mathbb{Z}$, where the positive values of m are sufficient to generate all the linearly independent solutions of (3.45).

The solutions to (3.46) are finite at $\theta = 0$ and $\theta = \pi$, which are associated Legendre functions of the first kind $P_n^m(\cos \theta)$ of degree n and order m , where $n = m, m + 1, \dots$

Note that, these functions are orthogonal

$$\int_{-1}^1 P_n^m(\cos \theta) P_{n'}^m(\cos \theta) d \cos \theta = \delta_{nn'} \frac{2}{2n + 1} \frac{(n + m)!}{(n - m)!}. \quad (3.51)$$

Now, if we introduce the dimensionless variable $\rho = kr$ and define the function

$Z = R\sqrt{\rho}$, (3.47) becomes

$$\rho \frac{d}{d\rho} \left(\rho \frac{dZ}{d\rho} \right) + \left[\rho^2 - \left(n + \frac{1}{2} \right)^2 \right] Z = 0, \quad (3.52)$$

which independent solutions are the Bessel functions of first and second kind J_ν and Y_ν , where the order $\nu = n + \frac{1}{2}$ is half-integral. Therefore, the linearly independent solutions to (3.47) are the spherical Bessel functions:

$$j_n(\rho) = \sqrt{\frac{\pi}{2\rho}} J_{n+\frac{1}{2}}(\rho), \quad (3.53)$$

$$y_n(\rho) = \sqrt{\frac{\pi}{2\rho}} Y_{n+\frac{1}{2}}(\rho), \quad (3.54)$$

where the constant factor $\sqrt{\frac{\pi}{2}}$ is introduced for convenience. The spherical Bessel functions satisfy the recurrence relations

$$z_{n-1}(\rho) + z_{n+1}(\rho) = \frac{2n+1}{\rho} z_n(\rho) \quad (3.55)$$

$$(2n+1) \frac{d}{d\rho} z_n(\rho) = n z_{n-1}(\rho) - (n+1) z_{n+1}(\rho) \quad (3.56)$$

where z_n is either j_n or y_n .

All the linear combinations of j_n and y_n is also a solution of (3.47). Therefore, we can take as fundamental solutions of (3.47) any two linearly independent combinations. In this case, we choose the spherical Bessel functions of the third kind or

Hankel functions:

$$h_n^{(1)}(\rho) = j_n(\rho) + iy_n(\rho) \quad (3.57)$$

$$h_n^{(2)}(\rho) = j_n(\rho) - iy_n(\rho) \quad (3.58)$$

By recombining the separated solution, we can now construct a complete basis for the generating functions that satisfy the scalar Helmholtz equation in spherical coordinates:

$$\phi_{emn} = \cos(m\phi)P_n^m(\cos\theta)z_n(kr), \quad (3.59)$$

$$\phi_{omn} = \sin(m\phi)P_n^m(\cos\theta)z_n(kr), \quad (3.60)$$

where z_n is any of the spherical Bessel functions j_n , y_n , $h_n^{(1)}$ or $h_n^{(2)}$. It is important to note here that, because of the completeness of the involved functions, any generating function $\psi(\mathbf{r})$ that satisfies the scalar Helmholtz equations in spherical coordinates can be projected the basis 3.59-3.60.

Using the spatial variable \mathbf{r} as the pilot vector, and projecting the generating function on the basis that solves the Helmholtz equation in spherical coordinates, we can

finally obtain the vector function basis which solves our problem:

$$\mathbf{M}_{emn} = \nabla \times (\mathbf{r}\psi_{emn}), \quad (3.61)$$

$$\mathbf{N}_{emn} = \frac{\nabla \times \mathbf{M}_{emn}}{k}, \quad (3.62)$$

$$\mathbf{M}_{omn} = \nabla \times (\mathbf{r}\psi_{omn}), \quad (3.63)$$

$$\mathbf{N}_{omn} = \frac{\nabla \times \mathbf{M}_{omn}}{k}. \quad (3.64)$$

Function 3.61-3.64 are known as Mie Vector Spherical Harmonics.

Next step is to project a plane x -polarized wave:

$$\mathbf{E}_i = E_0 e^{-i\rho \cos \theta} [\sin \theta \cos \varphi \hat{\mathbf{r}}(\theta, \varphi) + \cos \theta \cos \varphi \hat{\boldsymbol{\theta}}(\theta, \varphi) - \sin \varphi \hat{\boldsymbol{\phi}}(\varphi)] \quad (3.65)$$

on this basis:

$$\mathbf{E}_i = \sum_{m=0}^{\infty} \sum_{n=m}^{\infty} [B_{emn} \mathbf{M}_{emn} + B_{omn} \mathbf{M}_{omn} + A_{emn} \mathbf{N}_{emn} + A_{omn} \mathbf{N}_{omn}]. \quad (3.66)$$

Utilizing an equivalent of Fourier's trick and capitalizing on the orthogonality of the spherical harmonics, we can express B_{emn} as follows:

$$B_{emn} = \frac{\int_0^{2\pi} \int_0^{\pi} \mathbf{E}_i \cdot \mathbf{M}_{emn} \sin \theta d\theta d\varphi}{\int_0^{2\pi} \int_0^{\pi} |\mathbf{M}_{emn}|^2 \sin \theta d\theta d\varphi}. \quad (3.67)$$

The expressions for B_{omn} , A_{emn} , and A_{omn} can be derived in a similar way. The orthogonality of the functions implies that $B_{emn} = A_{omn} = 0$ for all m and n . Additionally, the remaining coefficients vanish except when $m = 1$, for the same reason.

The incident field is finite at the origin, which requires that $j_n(kr)$ is the appropriate spherical Bessel function in the generating functions ψ_{o1n} and ψ_{e1n} . Now, we shall append (1) to vector spherical harmonics for which the radial dependence of the generating functions is specified as j_n . Therefore, the expansion for \mathbf{E}_i is of the form

$$\mathbf{E}_i = \sum_{n=1}^{\infty} \left(B_{o1n} \mathbf{M}_{o1n}^{(1)} + A_{e1n} \mathbf{N}_{e1n}^{(1)} \right) \quad (3.68)$$

Now, considering that B_{o1n} and A_{e1n} can be expressed as

$$B_{o1n} = i^n E_0 \frac{2n+1}{n(n+1)}, \quad (3.69)$$

$$A_{e1n} = -i E_0 i^n \frac{2n+1}{n(n+1)}. \quad (3.70)$$

Thus, the expansion of a plane wave in spherical harmonics is given by

$$\mathbf{E}_i = E_0 \sum_{n=1}^{\infty} i^n \frac{2n+1}{n(n+1)} \left(\mathbf{M}_{o1n}^{(1)} - \mathbf{N}_{e1n}^{(1)} \right), \quad (3.71)$$

and its corresponding incident magnetic fields is

$$\mathbf{H}_i = -\frac{k}{\omega\mu} E_0 \sum_{n=1}^{\infty} i^n \frac{2n+1}{n(n+1)} \left(\mathbf{M}_{e1n}^{(1)} + i \mathbf{N}_{o1n}^{(1)} \right). \quad (3.72)$$

The fields in each region of the coated sphere still satisfy the vector Helmholtz equation. Consequently, each of them can be expressed as a projection onto Mie Vector Spherical Harmonics.

The expansion of the field in the nucleus ($\mathbf{E}_1, \mathbf{H}_1$) can thus be written as:

$$\mathbf{E}_1 = \sum_{n=1}^{\infty} E_n \left(\mathbf{c}_n \mathbf{M}_{o1n}^{(1)} - i \mathbf{d}_n \mathbf{N}_{e1n}^{(1)} \right), \quad (3.73)$$

$$\mathbf{H}_1 = -\frac{k_1}{\omega \mu_1} \sum_{n=1}^{\infty} E_n \left(\mathbf{d}_n \mathbf{M}_{e1n}^{(1)} + i \mathbf{c}_n \mathbf{N}_{o1n}^{(1)} \right), \quad (3.74)$$

where $E_n = i^n E_0 \frac{2n+1}{n(n-1)}$ and μ_1 is the permeability of the nucleus.

The scattered field ($\mathbf{E}_s, \mathbf{H}_s$) is given by

$$\mathbf{E}_s = \sum_{n=1}^{\infty} E_n \left(i \mathbf{a}_n \mathbf{N}_{e1n}^{(3)} - \mathbf{b}_n \mathbf{M}_{o1n}^{(3)} \right), \quad (3.75)$$

$$\mathbf{H}_s = \frac{k}{\omega \mu} \sum_{n=1}^{\infty} E_n \left(i \mathbf{b}_n \mathbf{N}_{o1n}^{(3)} + \mathbf{a}_n \mathbf{M}_{e1n}^{(3)} \right), \quad (3.76)$$

here we append (3) to the vector spherical harmonics for which the radial dependence of generating functions is specified as $h_n^{(1)}$.

Now, considering that in the shell both spherical Bessel functions j_n and y_n are finite, the expansion of the field ($\mathbf{E}_2, \mathbf{H}_2$) in this region is

$$\mathbf{E}_2 = \sum_{n=1}^{\infty} E_n \left(\mathbf{f}_n \mathbf{M}_{o1n}^{(1)} - i \mathbf{g}_n \mathbf{N}_{e1n}^{(1)} + \mathbf{v}_n \mathbf{M}_{o1n}^{(2)} - i \mathbf{w}_n \mathbf{N}_{e1n}^{(2)} \right), \quad (3.77)$$

$$\mathbf{H}_2 = -\frac{k_2}{\omega \mu_2} \sum_{n=1}^{\infty} E_n \left(\mathbf{g}_n \mathbf{M}_{e1n}^{(1)} + i \mathbf{f}_n \mathbf{N}_{o1n}^{(1)} + \mathbf{w}_n \mathbf{M}_{e1n}^{(2)} + i \mathbf{v}_n \mathbf{N}_{o1n}^{(2)} \right), \quad (3.78)$$

here we append (2) to the vector harmonics in which the radial dependence is specified as y_n .

The coefficients of the vector harmonics of these fields are not independent, and

their relations can be determined by applying the boundary conditions:

$$(\mathbf{E}_2 - \mathbf{E}_1)|_{r=a_1} \times \hat{\mathbf{r}}(\theta, \varphi) = 0, \quad (3.79)$$

$$(\mathbf{H}_2 - \mathbf{H}_1)|_{r=a_1} \times \hat{\mathbf{r}}(\theta, \varphi) = 0, \quad (3.80)$$

$$(\mathbf{E}_s + \mathbf{E}_1 - \mathbf{E}_2)|_{r=a_2} \times \hat{\mathbf{r}}(\theta, \varphi) = 0, \quad (3.81)$$

$$(\mathbf{H}_s + \mathbf{H}_1 - \mathbf{H}_2)|_{r=a_2} \times \hat{\mathbf{r}}(\theta, \varphi) = 0. \quad (3.82)$$

$$(3.83)$$

In the optical approximation we have that $\mu_1 = \mu_2 = \mu_3 = 1$ so the scattering coefficients \mathbf{a}_n and \mathbf{b}_n can be written as:

$$\mathbf{a}_n = \frac{\psi_n(y) [\psi'_n(m_2y) - \mathfrak{A}_n \chi'_n(m_2y)] - m_2 \psi'_n(y) [\psi_n(m_2y) - \mathfrak{A}_n \chi_n(m_2y)]}{\xi_n(y) [\psi'_n(m_2y) - \mathfrak{A}_n \chi'_n(m_2y)] - m_2 \xi'_n(y) [\psi_n(m_2y) - \mathfrak{A}_n \chi_n(m_2y)]}, \quad (3.84)$$

$$\mathbf{b}_n = \frac{\psi_n(y) [\psi'_n(m_2y) - \mathfrak{B}_n \chi'_n(m_2y)] - m_2 \psi'_n(y) [\psi_n(m_2y) - \mathfrak{B}_n \chi_n(m_2y)]}{m_2 \xi_n(y) [\psi'_n(m_2y) - \mathfrak{B}_n \chi'_n(m_2y)] - \xi'_n(y) [\psi_n(m_2y) - \mathfrak{B}_n \chi_n(m_2y)]}, \quad (3.85)$$

where

$$\mathfrak{A}_n = \frac{m_2 \psi_n(m_2x) \psi'_n(m_1x) - m_1 \psi'_n(m_2x) \psi_n(m_1x)}{m_2 \chi_n(m_2x) \psi'_n(m_1x) - m_1 \chi'_n(m_2x) \psi_n(m_1x)}, \quad (3.86)$$

$$\mathfrak{B}_n = \frac{m_2 \psi_n(m_1x) \psi'_n(m_2x) - m_1 \psi_n(m_2x) \psi'_n(m_1x)}{m_2 \chi'_n(m_2x) \psi_n(m_1x) - m_1 \psi'_n(m_2x) \chi_n(m_1x)}, \quad (3.87)$$

m_1 and m_2 are the relative refractive index of the nucleus and the shell related to the surrounding medium defined as $m_1 = \frac{n_1}{n_3}$ and $m_2 = \frac{n_2}{n_3}$, $x = ka_1$ and $y = ka_2$, while the Riccati-Bessel function χ is defined as $\chi_n(z) = -zy_n(z)$.

The solutions for the fields obtained through Mie theory seamlessly connect with the results of the quasistatic approximation when calculated for very small particles,

limiting the Mie expansion only to the first term \mathbf{a}_1 , which corresponds to the dipolar mode. In this region of the parameter space, the polarizability of the nanoparticle can be expressed as:

$$\alpha = 6\pi i \frac{\mathbf{a}_1}{k^3} \quad (3.88)$$

This can be analytically demonstrated by computing the scattered field using expression 3.75 and retaining only the scattering coefficient \mathbf{a}_1 while setting all others to zero. The resulting field takes the form of a dipolar field whose dipole moment is given by $\alpha \mathbf{E}_i$, where the polarizability α is defined as in expression 3.88.

3.3.1 Cross Sections

It is possible to relate the cross section of the nanoparticle to the scattering coefficients of Mie theory. A detailed derivation can be found in [8], yielding the result:

$$C_{ext} = \frac{2\pi}{k^2} \sum_{n=1}^{\infty} (2n+1) \operatorname{Re}\{\mathbf{a}_n + \mathbf{b}_n\} \quad (3.89)$$

$$C_{sca} = \frac{2\pi}{k^2} \sum_{n=1}^{\infty} (2n+1) (|\mathbf{a}_n|^2 + |\mathbf{b}_n|^2) \quad (3.90)$$

$$C_{abs} = C_{ext} - C_{sca} \quad (3.91)$$

With these formulas, along with their counterparts calculated in the previous chapter, we now possess all the necessary tools to address the scattering problem, encompassing scenarios with both small and large particles relative to the wavelength of the incident field.

3.4 Rupture of the quasistatic limit

For small particles, the results obtained through Mie theory converge to those calculated in the quasistatic limit. However, for larger particles, the two methods yield divergent results. This discrepancy arises due to significant phase changes induced by the incident field throughout the particle volume, giving rise to higher-order modes. Consequently, the quasistatic regime breaks down, as it is incapable of capturing the effects of an inhomogeneous field. Therefore, when dealing with larger particles, a rigorous electromagnetic approach such as Mie theory becomes essential to accurately describe the scattering phenomenon.

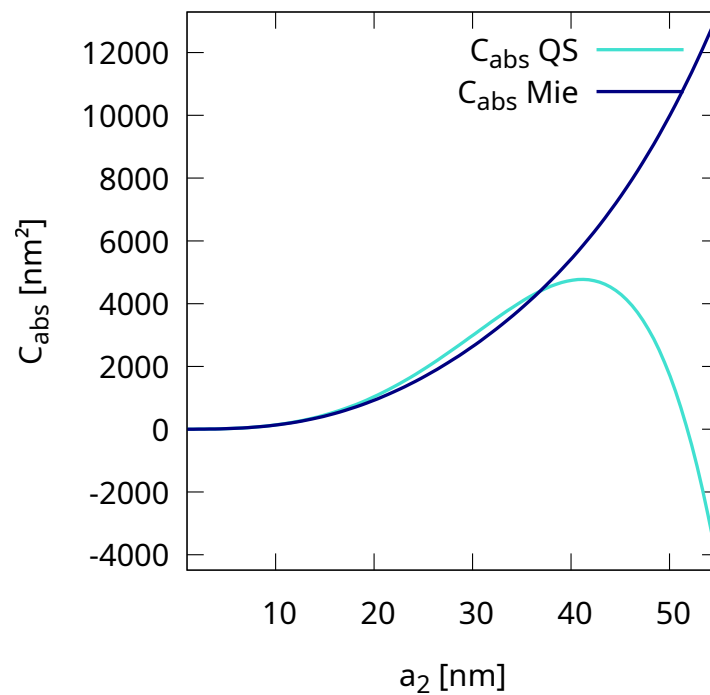


Figure 3.2: Absorption Cross Section for a nano-shell particle with $\rho = 0.8$ and $G = 0$, in which $\lambda = 590[\text{nm}]$ is fixed.

The breakdown of the quasistatic limit becomes evident when examining the cross sections for larger particles as in Figure 3.2. In the quasistatic limit applied to larger particles, a notable outcome is a negative absorption cross section. This implies that the scattering cross section surpasses the extinction cross section, suggesting that the nanoparticle scatters more light than it receives.

While such a result is not entirely implausible when dealing with nanoparticles incorporating gain elements, it still lacks physical coherence when the gain quantity falls below the emission threshold. In this regime, the nanoparticle should still behave as an absorber. This becomes particularly evident when there is no gain added to the system, as in the case illustrated in Figure 3.3. Consequently, this outcome underscores the limitation of the quasistatic approximation in accurately describing the behavior of larger particles. Furthermore, the emergence of a negative absorption cross section (below the emission threshold) serves as a critical indicator that the quasistatic limit is not a suitable model for the case under consideration.

The system discussed in this thesis, a nanoshell, adds an extra layer of complexity to the parameter space, making the applicability of the quasistatic limit more challenging. A nanoshell consists of a coated sphere with a dielectric core containing gain elements and a metal shell. This introduces additional factors that can influence the quasistatic limit's validity. The thickness of the shell, which affects the amount of metal and the level of gain in the system, becomes just as crucial as the particle size in determining the effectiveness of the quasistatic approach.

In specific terms: a nano-shell characterized by a thick shell (i. e., a small ρ) contains a higher amount of metal. Consequently, it surpasses the range of validity

for the quasistatic limit at a smaller size compared to a nano-shell with a thin shell (i. e., a larger ρ).

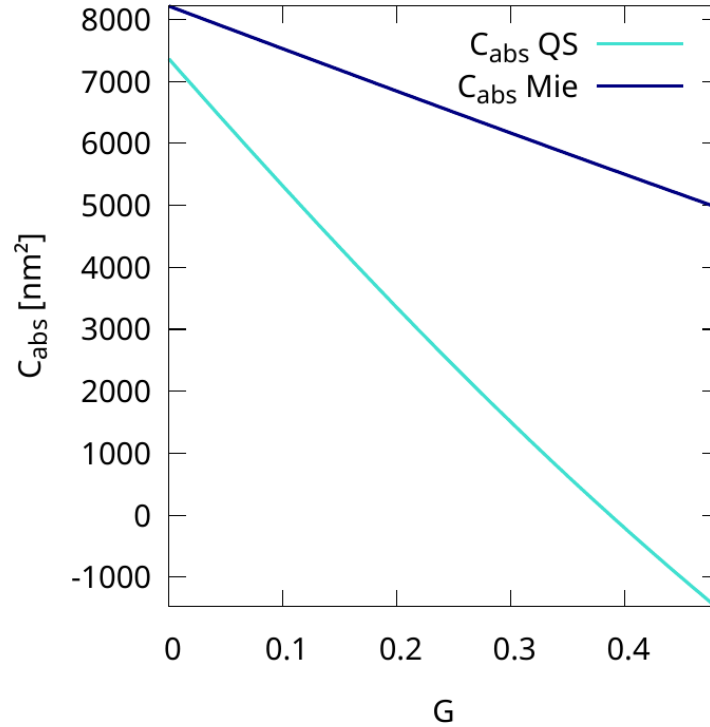


Figure 3.3: Absorption Cross Section for a nano-shell particle with external radius of 40 [nm] and $\rho = 0.8$, in which $\lambda = 626$ [nm] is fixed and G is below the emission threshold.

Furthermore, the introduction of gain into the system can lead to a negative absorption cross-section, even below the emission threshold when calculated using the quasistatic approximation. On the contrary, the absorption cross-section calculated using Mie Theory only becomes negative above the emission threshold. This indicates that the quasistatic approximation breaks down for particles of a size at which a passive nanoshell could be accurately described within the quasistatic limit.

This phenomenon occurs because the inclusion of active elements enhances the

electromagnetic field around the nanoshell, causing it to behave as if it were a larger nanoparticle from an electromagnetic perspective.

Chapter 4

Time dependent model

In the search for applications like SPASER and amplification effects, the simplest system to study involves a single spherical metal nanoparticle that is significantly smaller than the resonant optical field wavelength, placed within an infinitely amplifying medium [31]. However, this setup faced an issue of non-uniformity in the amplified field [32] when the gain exceeded the emission threshold. This behavior is reminiscent of the Spatial Hole Burning phenomenon observed in Laser Physics.

The non-uniformity in the amplified field arises from the non-homogeneous distribution of field intensity within the gain medium. The gain medium is in fact located in the solvent surrounding the plasmonic nanoparticle, and the plasmonic field there has a dipolar nature. This non-uniformity leads to an uneven consumption of the population inversion in the gain medium, resulting in non-uniform field amplification and an undesirable cascade of modes.

However, in the spherical nano-shell configuration, which is the primary focus of this thesis, the gain elements are located within the core of the nano-shell. Consequently, especially in the quasi-static limit, the field within the core remains uniform. As a result, the depletion of population inversion induced by the field in the gain medium is also uniform.

This section introduces a hybrid (quantum and classical) quasi-static model that utilizes dynamic constitutive equations, similar to those described in [32]. However, in this model, these equations are interconnected through boundary conditions that are specific to the spherical nano-shell geometry. This approach takes advantage of the field's uniformity in the gain region, providing a comprehensive spectral description of the electromagnetic response of these systems that extends beyond the emission threshold.

To achieve this, we will consider the time evolution equations for the gain medium and the metal introduced in Section 2. These equations are as follows:

$$\frac{d\mathbf{\Pi}_h}{dt} - \left[i(\omega - \omega_{21}) - \frac{1}{\tau_2} \right] \mathbf{\Pi}_h = -\frac{i\varepsilon_0 G N}{\tau_2} \frac{N}{\tilde{N}} \mathbf{E}_h, \quad (4.1)$$

$$\frac{dN}{dt} + \frac{N - \tilde{N}}{\tau_1} = -\frac{i}{2n\hbar} (\mathbf{\Pi}_h \cdot \mathbf{E}_h^* - \mathbf{\Pi}_h^* \cdot \mathbf{E}_h), \quad (4.2)$$

$$\frac{d\mathbf{\Pi}_m}{dt} - \frac{\omega(\omega + 2i\gamma)}{2(\gamma - i\omega)} \mathbf{\Pi}_m = \frac{\varepsilon_0 \omega_{\text{pl}}^2}{2(\gamma - i\omega)} \mathbf{E}_m. \quad (4.3)$$

We will model this system by applying the quasistatic approximation and considering the radial and tangential boundary conditions for the potential. This will allow us to obtain the following expressions for the associated potentials of the electric field and

polarizations, denoted as Φ and Ψ respectively:

$$\Phi_h(r, \theta, t) = \left(\frac{\tilde{p}_2}{\rho^3 a_2^3} + \frac{p_3 - \tilde{p}_2}{a_2^3} - E_0 \right) r \cos(\theta) \quad (4.4)$$

$$\Phi_m(r, \theta, t) = \left(\frac{p_3 - \tilde{p}_2}{a_2^3} - E_0 \right) r \cos(\theta) + \tilde{p}_2 \frac{\cos(\theta)}{r^2} \quad (4.5)$$

$$\Phi_s(r, \theta, t) = -E_0 r \cos(\theta) + p_3 \frac{\cos(\theta)}{r^2} \quad (4.6)$$

$$\Psi_h(r, \theta, t) = q_0 r \cos(\theta) \quad (4.7)$$

$$\Psi_m(r, \theta, t) = q_1 r \cos(\theta) + q_2 \frac{\cos(\theta)}{r^2} \quad (4.8)$$

To solve the equation system (4.1)-(4.3) we need to find the radial components for the electric field and polarizations in all of the regions.

$$E_h^r = -\frac{\partial \Phi(r, \theta)}{\partial r} = \left(E_0 - \frac{\tilde{p}_2}{\rho^3 a_2^3} - \frac{p_3 - \tilde{p}_2}{a_2^3} \right) \cos(\theta) \quad (4.9)$$

$$E_m^r = -\frac{\partial \Phi_m(r, \theta)}{\partial r} = \left[E_0 \cos(\theta) - \frac{p_3 - \tilde{p}_2}{a_2^3} \right] \cos(\theta) + 2\rho^3 \frac{\cos(\theta)}{r^3} \quad (4.10)$$

$$E_s^r = -\frac{\partial \Phi_h(r, \theta)}{\partial r} = E_0 \cos(\theta) + 2p_3 \frac{\cos(\theta)}{r^3} \quad (4.11)$$

$$\Pi_h^r = -\frac{\partial \Psi_h(r, \theta)}{\partial r} = -q_0 \cos(\theta) \quad (4.12)$$

$$\Pi_m^r = -\frac{\partial \Psi_m(r, \theta)}{\partial r} = -q_1 \cos(\theta) + 2q_2 \frac{\cos(\theta)}{r^3} \quad (4.13)$$

Replacing in the equation system (4.1)-(4.3) we can rewrite it as

$$\frac{dq_0}{dt} - \left[i(\omega - \omega_{21}) - \frac{1}{\tau_2} \right] q_0 = \frac{iGN}{\tau_2 \tilde{N}} \left(E_0 - \frac{\tilde{p}_2}{\rho^3 a_2^3} - \frac{p_3 - \tilde{p}_2}{a_2^3} \right) \quad (4.14)$$

$$\frac{dq_1}{dt} - \frac{\omega(\omega + 2i\gamma)}{2(\gamma - i\omega)} q_1 = \frac{1}{2(\gamma - i\omega)} \left(\frac{p_3 - \tilde{p}_2}{a_2^3} - E_0 \right) \quad (4.15)$$

$$\frac{dq_2}{dt} - \frac{\omega(\omega + 2i\gamma)}{2(\gamma - i\omega)} q_2 = \frac{1}{2(\gamma - i\omega)} \tilde{p}_2 \quad (4.16)$$

To simplify the system we define the following parameters

$$\Omega_H = i(\omega - \omega_{21}) - \frac{1}{\tau_2} \quad (4.17)$$

$$\Omega_P = \frac{\omega(\omega + 2i\gamma)}{2(\gamma - i\omega)} \quad (4.18)$$

$$\Gamma_P = \frac{1}{2(\gamma - i\omega)} \quad (4.19)$$

$$\tilde{G} = -\frac{iG}{\tau_2} \quad (4.20)$$

Defining $p_2 = \frac{\tilde{p}_2}{\rho^3}$ and $\tilde{q}_2 = \frac{q_2}{\rho^3}$, hence when normalizing by a_2 we get a system of equations determining the time evolution of the coefficients $q_{0,1,2}$:

$$\frac{dq_0}{dt} - \Omega_H q_0 = \tilde{G} p_0 \quad (4.21)$$

$$\frac{dq_1}{dt} - \Omega_P q_1 = \Gamma_P p_1 \quad (4.22)$$

$$\frac{dq_2}{dt} - \Omega_P q_2 = \Gamma_P p_2 \quad (4.23)$$

where

$$p_1 = p_3 - \rho^3 p_2 - E_0; \quad (4.24)$$

$$p_0 = p_1 + p_2. \quad (4.25)$$

Note that, the time evolution population inversion N in equation 4.21 is determined by:

$$\frac{dN}{dt} + \frac{N - \tilde{N}}{\tau_1} = \frac{\text{Im} \{q_0 p_0^*\}}{n\hbar}, \quad (4.26)$$

Relations 4.21-4.23 represent a linear system whose solutions for p_0 , p_1 , p_2 and p_3 are linear combinations of q_0 , q_1 , q_2 and E_0 , namely:

$$p_0 = p_{00}q_0 + p_{01}q_1 + p_{02}q_2 + p_{03}E_0, \quad (4.27)$$

$$p_1 = p_{10}q_0 + p_{11}q_1 + p_{12}q_2 + p_{13}E_0, \quad (4.28)$$

$$p_2 = p_{20}q_0 + p_{21}q_1 + p_{22}q_2 + p_{23}E_0, \quad (4.29)$$

$$p_3 = p_{30}q_0 + p_{31}q_1 + p_{32}q_2 + p_{33}E_0. \quad (4.30)$$

Therefore, we need to find the parameters p_0 , p_1 and p_2 . Which will be done by applying the boundary conditions for the polarizations

$$\mathbf{P}_h = \varepsilon_b \mathbf{E}_h + \mathbf{\Pi}_h \quad (4.31)$$

$$\mathbf{P}_m = \varepsilon_\infty \mathbf{E}_m + \mathbf{\Pi}_m \quad (4.32)$$

$$\mathbf{P}_s = \varepsilon_s \mathbf{E}_s \quad (4.33)$$

Which are:

$$[\varepsilon_b E_h^r + \Pi_h^r]_{\rho=a_1} = [\varepsilon_\infty E_m^r + \Pi_m^r]_{\rho=a_1} \quad (4.34)$$

$$[\varepsilon_\infty E_m^r + \Pi_m^r]_{\rho=a_2} = [\varepsilon_s E_s^r]_{\rho=a_2}. \quad (4.35)$$

Obtaining

$$p_{00} = -\frac{(\varepsilon_\infty + 2\varepsilon_s) + 2\rho^3(\varepsilon_\infty - \varepsilon_s)}{D_1} \quad (4.36)$$

$$p_{01} = -2(1 - \rho^3) \frac{\varepsilon_\infty - \varepsilon_s}{D_1} \quad (4.37)$$

$$p_{02} = -2(1 - \rho^3) \frac{\varepsilon_\infty + 2\varepsilon_s}{D_1} \quad (4.38)$$

$$p_{03} = -9 \frac{\varepsilon_s \varepsilon_\infty}{D_1} \quad (4.39)$$

$$p_{10} = 2\rho^3 \frac{\varepsilon_s - \varepsilon_\infty}{D_1} \quad (4.40)$$

$$p_{11} = -\frac{\rho^3(\varepsilon_b + 2\varepsilon_s) + (1 - \rho^3)(\varepsilon_b + 2\varepsilon_\infty)}{D_1} \quad (4.41)$$

$$p_{12} = 2\rho^3 \frac{\varepsilon_b + 2\varepsilon_s}{D_1} \quad (4.42)$$

$$p_{13} = -3 \frac{\varepsilon_s(\varepsilon_b + 2\varepsilon_\infty)}{D_1} \quad (4.43)$$

$$(4.44)$$

$$p_{20} = -\frac{\varepsilon_\infty + 2\varepsilon_s}{D_1} \quad (4.45)$$

$$p_{21} = \frac{\varepsilon_b + 2\varepsilon_s}{D_1} \quad (4.46)$$

$$p_{22} = -2\frac{(\varepsilon_\infty + 2\varepsilon_s) + \rho^3(\varepsilon_b - \varepsilon_\infty)}{D_1} \quad (4.47)$$

$$p_{23} = 3\frac{\varepsilon_s(\varepsilon_b - \varepsilon_\infty)}{D_1} \quad (4.48)$$

where

$$D_1 = (\varepsilon_\infty + 2\varepsilon_s)(\varepsilon_b + 2\varepsilon_\infty) + 2\rho^3(\varepsilon_b - \varepsilon_\infty)(\varepsilon_\infty - \varepsilon_s) \quad (4.49)$$

As evidence of the solidity of this model, one can use it to calculate the steady state solutions for quantities q_0 , q_1 and q_2 ; substitute them into 4.30 and find that the normalized polarizability $\alpha/(4\pi\varepsilon_s a^3) = p_3/E_0$ converges to the classical steady-state formula:

$$\frac{(\varepsilon_m - \varepsilon_s)(\varepsilon_h + 2\varepsilon_m) + \rho^3(\varepsilon_h - \varepsilon_m)(\varepsilon_s + 2\varepsilon_m)}{(\varepsilon_m + 2\varepsilon_s)(\varepsilon_h + 2\varepsilon_m) + 2\rho^3(\varepsilon_m - \varepsilon_s)(\varepsilon_h - \varepsilon_m)}, \quad (4.50)$$

here ε_m is the Drude's metal permittivity 2.24 while ε_h is defined by expression 2.12.

This result couples with what we discussed in the previous section about the permittivities of the materials. It means that as long as steady-state

$$\frac{dq_i}{dt} = 0 \quad \text{for } i = 0, 1, 2 \quad (4.51)$$

can be reached, the use the equation 4.50 for the polarizability of a nano shell, including the appropriate steady state formula for the permittivities of metal and di-

electric is perfectly legit even when gain is added to the system.

However, in the following we will show that condition 4.51 breaks when $G \geq G_{\text{th}}$ which is when the nanoparticle enters its emissive regime and a richer phenomenology arise. Nevertheless, even when the emissive regime is reached, the homogeneity of the field in the nano-shell's core gives us the tactical advantage of preventing any Spatial Hole Burning mode-cascade, this way allowing to find complete numerical solutions for system compose of 4.21, 4.22, 4.23 and 4.26.

Afterwards, can use the coefficients p_{ij} to define the matrix \mathbf{A} :

$$\mathbf{A} = \begin{bmatrix} \tilde{G}Np_{00} + \Omega_H & \tilde{G}Np_{01} & \tilde{G}Np_{02} \\ \Gamma_P p_{10} & \Omega_P + \Gamma_P p_{11} & \Gamma_P p_{12} \\ \Gamma_P p_{20} & \Gamma_P p_{21} & \Omega_P + \Gamma_P p_{22} \end{bmatrix}, \quad (4.52)$$

and the vector \mathbf{b} :

$$\mathbf{b} = (\tilde{G}p_{03}, \Gamma_P p_{13}, \Gamma_P p_{23})E_0. \quad (4.53)$$

Using \mathbf{A} and \mathbf{b} and reorganizing the coefficients q_i in the vector $\tilde{\mathbf{q}}$:

$$\tilde{\mathbf{q}} = (q_0, q_1, q_2), \quad (4.54)$$

system of equations 4.21-4.23 can be rewritten in the form:

$$\frac{d\tilde{\mathbf{q}}}{dt} = \mathbf{A}\tilde{\mathbf{q}} + \mathbf{b}, \quad (4.55)$$

$$\frac{dN}{dt} + \frac{N - \tilde{N}}{\tau_1} = \frac{\text{Im}\{q_0 p_0^*\}}{n\hbar}. \quad (4.56)$$

Solutions of the system of equations 4.55-4.56 present inherent time dependence, because of the selected initial conditions. In this case, we considered a non-excited system as initial condition, i.e $\mathbf{q}(0) = (0, 0, 0)$, where $t = 0$ corresponds to the moment when the exciting probe field $\tilde{\mathbf{E}}_0$ is activated.

In the upcoming sections, we will investigate the system's dynamic characteristics both below and above the emission threshold. It's important to highlight that, due to the resonant nature of these systems, the time evolution of this parameter shows considerable sensitivity to the chosen frequency. Therefore, we computed this temporal behavior for $\omega = 2.811$ eV, a value close to but not exactly equal to the singular resonance frequency ω_{sp} .

4.1 Below the Emission Threshold

We initiated our calculations with the pump switched off. As illustrated in figure 4.1, the solutions for q_0 , q_1 and q_2 swiftly approaches a non-pumped steady state within a few picoseconds. At $t = 10$ [ps], upon activating the pump (i. e. setting a G value higher than zero), the system subsequently achieves its *pumped steady state* (again in under 10 ps). It is clear from the results that the value of q_0 is two orders of magnitude less than that of q_1 and q_2 . This indicates that the dynamic aspect of the polarization in the gain-enriched silica core is much smaller compared to its counterpart in the silver shell.

It is crucial to note that in this regime, the analytical and numerical solutions exhibit complete alignment. This is because the field intensity in the gain-rich re-

gion stays low enough, preventing the activation of the saturation term (which is not considered in the linear analytical solution).

To validate the solutions illustrated in Figure 4.1, it is important to highlight that when these solutions are inserted into Equation 4.30, they enable the computation of a time-varying polarizability, denoted as $\alpha(t)/(4\pi\epsilon_s a^3)$ and defined as $p_3(t)/E_0$. The temporal evolution of this quantity is shown in Figure 4.2(a), allowing for a comparison with the spectrum of the pumped steady state of the same parameter calculated using Equation 4.50 and presented in Figure 4.2(b). To facilitate the comparison, the frequency utilized for the time evolution calculation is marked by a vertical blue line. The time-dependent polarizability rapidly converges to the steady state computed using the well-established steady-state formula. This suggests that, under the emission threshold (and within the small-signal range), it is entirely valid to represent the impact of gain by replacing in the expression for the permittivity of the gain medium into the steady-state formula for polarizability.

4.2 Above the Emission Threshold

The scenario undergoes a significant change with even a slight increased in the introduced gain beyond the threshold G_{th} . In the computation depicted in Figure 4.3, for instance, we utilized a gain value of merely $1.01G_{\text{th}}$; nevertheless, the resulting amplification is orders of magnitude higher. It is noteworthy that the duration for the system to reach saturation is considerably prolonged compared to the typical times required in the sub-emissive scenario to converge to a steady state. This is attributed

to the specific parameters chosen, particularly the deliberately low amplitude E_0 of the stimulating field, selected to keep the system within the small-signal regime. In the variable set used for the calculation presented in Figure 4.3, saturation occurs between 250 and 300 picoseconds. This timeframe also signifies when the numerical solution of the system (considering saturation) diverges from the analytical solution (which disregards saturation). Beyond this point, non-saturated time-dynamic models, such as the ones presented in [31] and [27], become ineffective.

It is crucial to emphasize that neither the analytical nor the numerical solutions achieve a genuine steady state; they seem to persistently oscillate at a constant frequency indefinitely. This suggests that when solved for a level of gain surpassing the emission threshold, the solution of system 4.55 (following an initial transient) takes on the following structure:

$$\tilde{\mathbf{q}}(t) = \tilde{\mathbf{Q}}e^{-i\Omega t}, \quad (4.57)$$

Where $\tilde{\mathbf{Q}}$ is a constant, complex vector amplitude and Ω the oscillation frequency. This pattern can be attributed to the saturation term relying on the intensity of the field in the gain region rather than its amplitude. Consequently, it guarantees a stable state exclusively for the intensity of the fields and polarizations, not their amplitudes. It is essential to recall that in this context, $\tilde{\mathbf{q}}(t)$ already represents a complex, slowly varying amplitude. Consequently, solutions in this form are physically valid only in the scenario where $\Omega \ll \omega$. Through our simulations, we determined Ω using Fourier analysis for each of our numerical solutions. We observed that Ω is dependent on the exciting field frequency ω and, within our specified parameter range, it falls within the interval of $-0.2 \text{ eV} < \hbar\Omega < 0.2 \text{ eV}$. This indicates that the rotating wave approximation introduced in our model is suitable when working in the visible

range (i.e., 1.63 to 3.26 eV). However, it also suggests that nanoparticles resonating in the infrared may necessitate a different approach.

In Figure 4.4(a), we depict the super-emissive behavior of the time-dependent polarizability. Notably, (I) the polarizability never appears to reach a genuine steady state, and (II) its behavior is distinctly different from the steady state calculated using Equation 4.50 and presented in Figure 4.4(b) for reference. This suggests that above the emission threshold, employing expression for the permittivity of the gain medium in the steady-state polarizability, formula 4.50 is not physically accurate and may lead to artifacts.

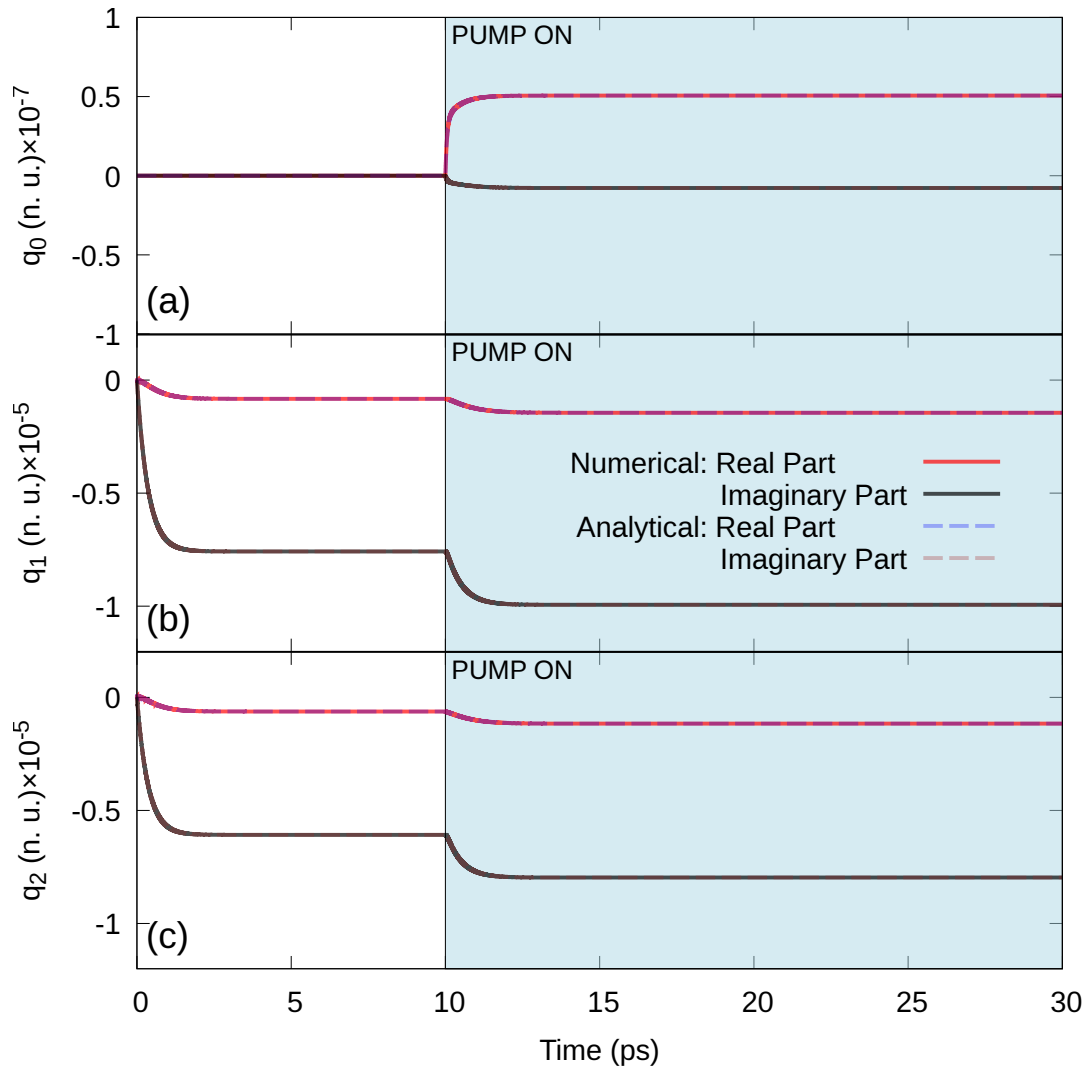


Figure 4.1: Analytical and Numerical solutions calculated for $\hbar\omega = 2.811$ eV with a sub-emissive gain quantity ($G = 0.033$). The pump is switched on at $t = 10$ ps. We present the real and imaginary part of: (a) q_0 ; (b) q_1 ; (c) q_2 . The numerical solutions are presented in continuous lines (red and black respectively for the real and imaginary part) while the analytical solutions are presented in dashed lines (purple and brown respectively for the real and imaginary part).

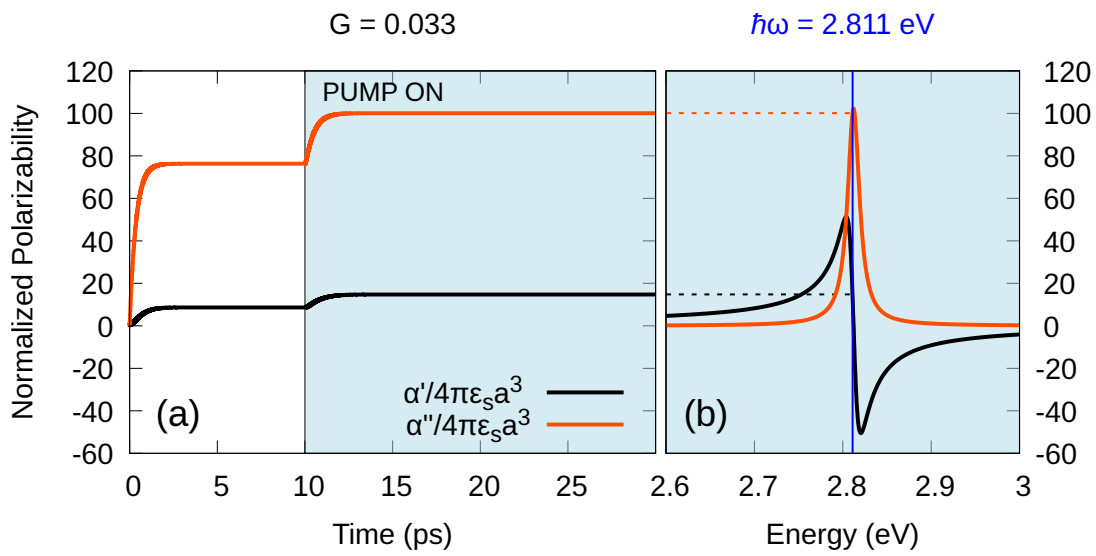


Figure 4.2: Normalized polarizability with a sub-emissive gain quantity ($G = 0.033$). The real and imaginary parts are shown as black and orange lines, respectively. (a) Time dependence calculated for $\hbar\omega = 2.811$ eV. (b) Steady-state spectrum. A blue line at $\hbar\omega = 2.811$ eV serves as a reference.

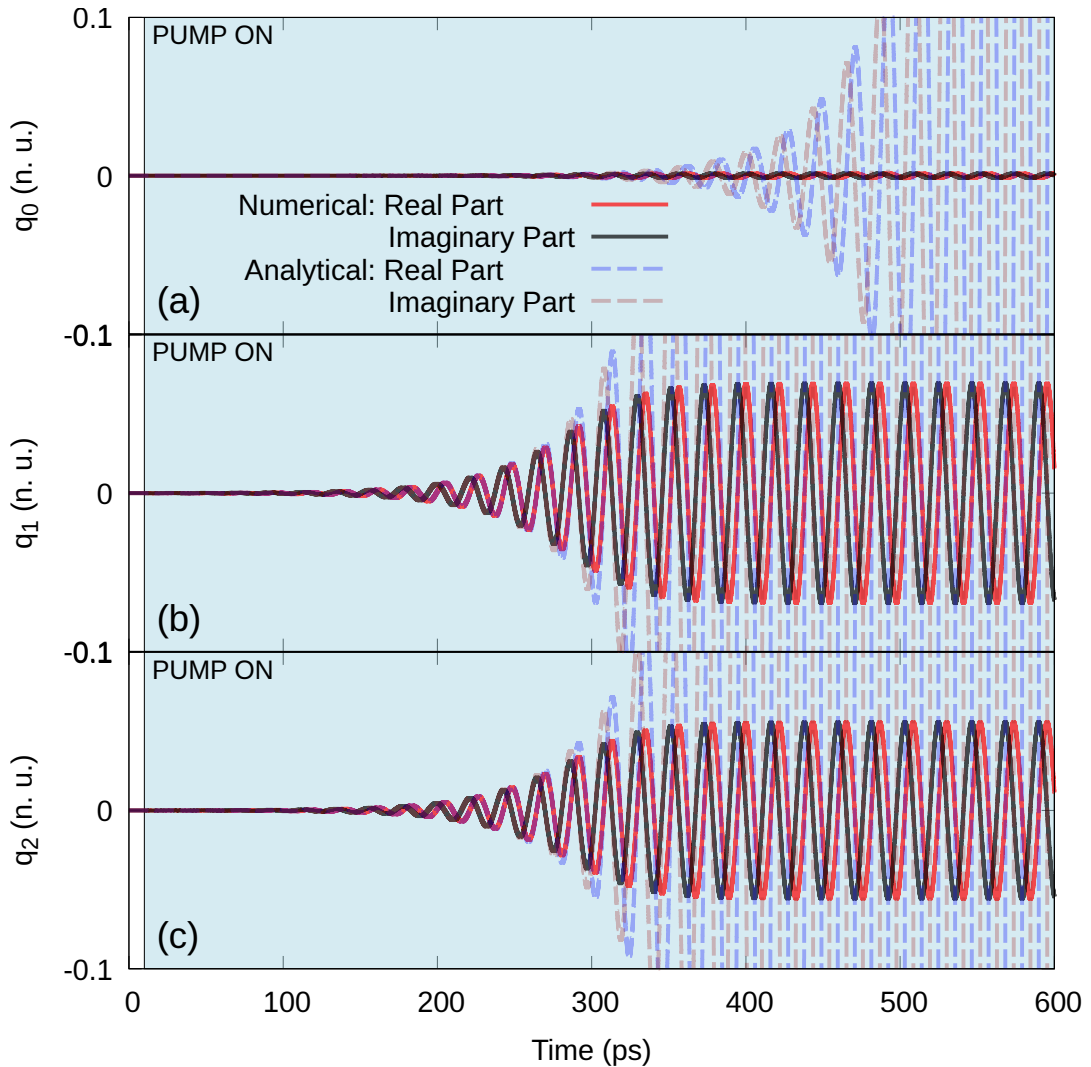


Figure 4.3: Analytical and Numerical solutions at $\hbar\omega = 2.811$ eV with a super-emissive gain quantity ($G \sim 0.136$). The pump is switched on at $t = 10$ ps. Time evolution for the real and imaginary part of: (a) q_0 ; (b) q_1 ; (c) q_2 . The numerical solutions are presented in continuous lines (red and black respectively for the real and imaginary part) while the analytical solutions are presented in dashed lines (purple and brown respectively for the real and imaginary part).

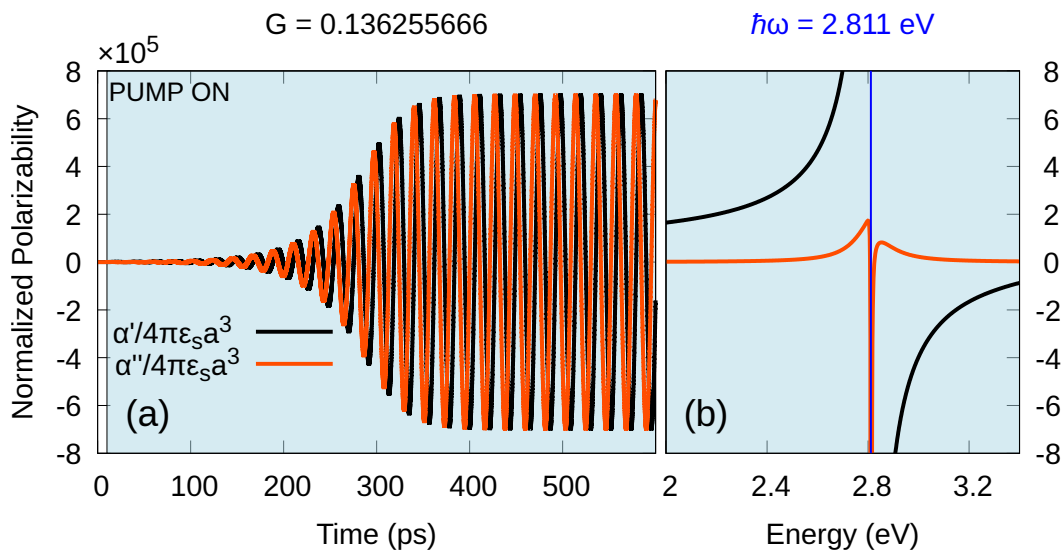


Figure 4.4: Normalized polarizability with a super-emissive gain quantity ($G \sim 0.136$). The real and imaginary parts are shown as black and orange lines, respectively. (a) Time dependence calculated for $\hbar\omega = 2.811 \text{ eV}$. (b) Steady-state spectrum. A blue line at $\hbar\omega = 2.811 \text{ eV}$ serves as a reference.

Chapter 5

Thermal Behavior

Recalling that the plasmonic nanoparticle as supporting plasmonic resonance of localized surface present interesting phenomenons such as heating. The thermal behavior of a plasmonic nanoparticle in recent years has been a interesting topic in which several researches are focused. This interest in thermo-plasmonics had lead to the development of noble applications like the plasmonic photothermal cancer therapy and useful technological applications like the improvement in optical trap efficiency.

5.1 Heat dissipated by a nanoparticle

Regardless the size of the nanoparticle, the polarizability is responsible for a resonance both in absorption and scattering. Recalling that the absorption cross section

quantifies the amount of luminous energy that is absorbed by the nanoparticle, we can model the power dissipated as heat by the nanoparticle as

$$\tilde{Q} = C_{abs}I, \quad (5.1)$$

where I is the intensity of the incident light.

5.2 Temperature in a nanosphere

We begin our analysis by considering the simplest configuration, i.e. a nanosphere particle. This is a model that has been widely studied analytically and experimentally. In this case, we will base our work on the one developed by Baffou [6].

Let us consider a metal nanoparticle of radius a in which the temperature inside and outside the sphere is given by:

For $r < a$

$$T_1(r) = \frac{\tilde{Q}}{4\pi a K_2} \left[1 + \frac{K_2}{2K_1} \left(1 - \frac{r^2}{a^2} \right) \right] + T_0, \quad (5.2)$$

for $r > a$

$$T_2(r) = \frac{\tilde{Q}}{4\pi K_2 r} + T_0. \quad (5.3)$$

where r is the radial distance, \tilde{Q} is the power absorbed as heat, K_1 and K_2 are the thermal conductivity of the nanoparticle and the surrounding medium respectively, and T_0 is the laboratory temperature. Let us analyze a graph for the temperature inside and outside a gold nanoparticle of 10 [nm] of radius surrounded by water.

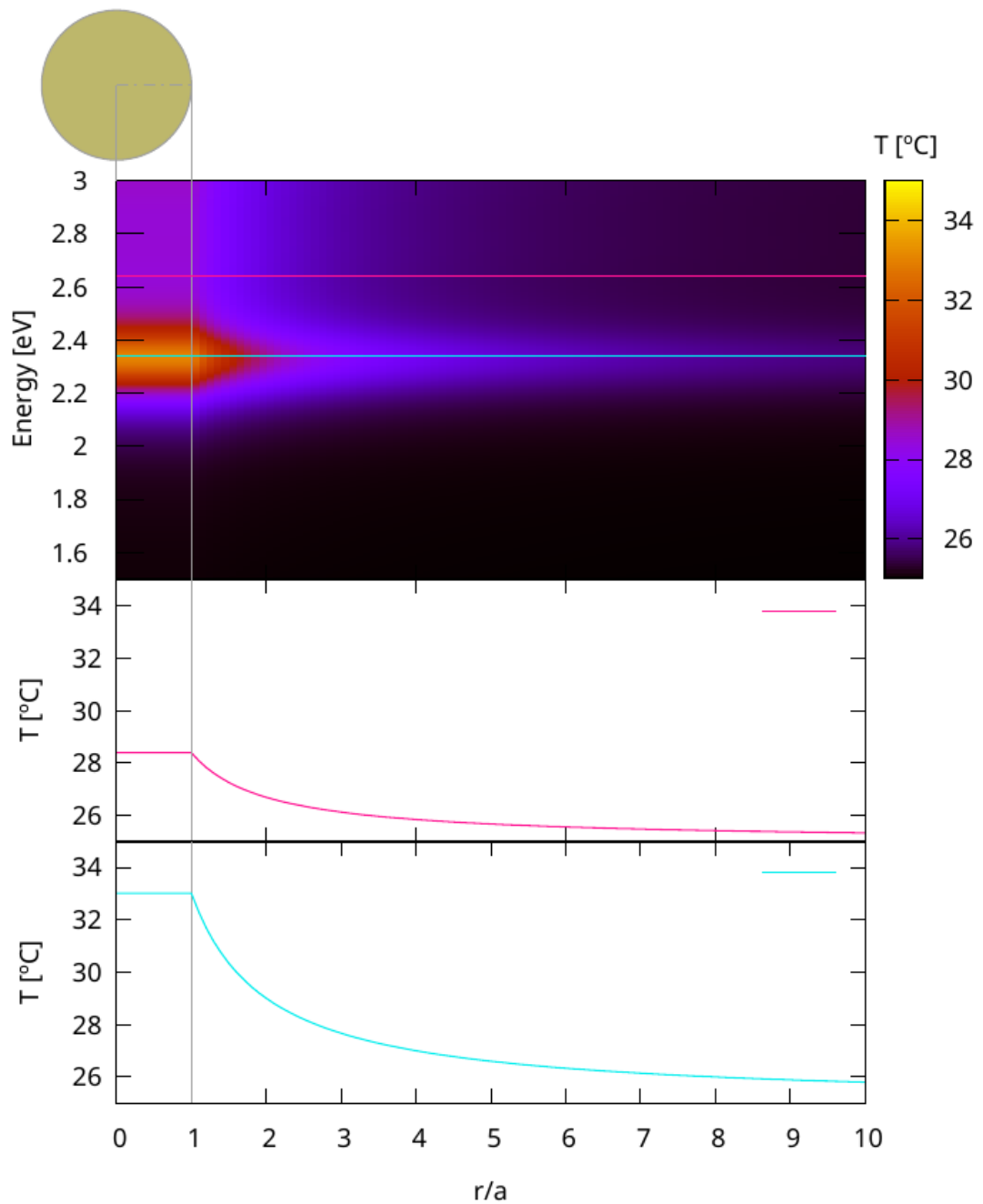


Figure 5.1: Temperature inside and outside a gold nanoparticle with radius 10 [nm] in the spectrum from 1.5 [eV] to 3 [eV], also we present the temperature in function of the radial distance for 2.639324 [eV] (dark pink line) and 2.339324 [eV] (cyan line)

Given an incident wavelength of $\lambda = 530$ [nm] which is $\hbar\omega = 2.339324$ [eV] we can observe that near the plasmonic resonance it is possible to achieve temperatures of 10 [°C] greater than the laboratory temperature, which in this case is fixed as 25 [°C]. Meanwhile, for a incident wavelength that is far from the resonant frequency we just obtain an increment of approximately 3 [°C] in the temperature.

Now, it will be interesting to extend this model for nano-shell particles since this configurations are used in medical applications.

5.3 Temperature in a nano-shell

Considering the heat transfer equation

$$\nabla \cdot [-K(\mathbf{r})\nabla T(\mathbf{r}, t)] + \rho(\mathbf{r})c(\mathbf{r})\frac{\partial T(\mathbf{r}, t)}{\partial t} = Q(\mathbf{r}, t), \quad (5.4)$$

where $T(\mathbf{r}, t)$ is the local temperature, $K(\mathbf{r})$ is the thermal conductivity, $\rho(\mathbf{r})$ is the mass density of the nanoparticle, $c(\mathbf{r})$ is the specific heat of the nanoparticle and $Q(\mathbf{r}, t)$ is the heat coming out from the energy dissipation inside the nanoparticle.

Since our system is a nano-shell it has spherical symmetry, i.e $f(\mathbf{r}) = f(r)$, we rewrite the equation as

$$-K(r)\nabla^2 T(r, t) + \rho(r)c(r)\frac{\partial T(r, t)}{\partial t} = Q(r, t). \quad (5.5)$$

Therefore, recalling the Laplacian in spherical coordinates and assuming that the

heat energy is constant in time, i.e $Q(r, t) = Q(r)$, we obtain

$$-K(r) \frac{1}{r^2} \frac{\partial}{\partial r} \left[r^2 \frac{\partial T(r, t)}{\partial r} \right] + \rho(r)c(r) \frac{\partial T(r, t)}{\partial t} = Q(r). \quad (5.6)$$

Now, we solve the equation inside and outside the nanoparticle.

For $0 \leq r \leq a_1$, with $Q(r) = 0$ and $K(r) = K_1$, we have

$$-K_1 \frac{1}{r^2} \frac{\partial}{\partial r} \left[r^2 \frac{\partial T(r, t)}{\partial r} \right] + \rho_1 c_1 \frac{\partial T(r, t)}{\partial t} = 0, \quad (5.7)$$

thus we find the steady state solution:

$$T_1(r) = \frac{c_1}{r} + c_2. \quad (5.8)$$

For $a_1 \leq r \leq a_2$, with $Q(r) = q$, $K(r) = K_2$, we have

$$-K_2 \frac{1}{r^2} \frac{\partial}{\partial r} \left[r^2 \frac{\partial T(r, t)}{\partial r} \right] + \rho_2 c_2 \frac{\partial T(r, t)}{\partial t} = q, \quad (5.9)$$

thus we find the steady state solution:

$$T_2(r) = -\frac{qr^2}{6K_2} + \frac{c_3}{r} + c_4. \quad (5.10)$$

For $r \geq a_2$, with $Q(r) = 0$ and $K(r) = K_3$, we have

$$-K_3 \frac{1}{r^2} \frac{\partial}{\partial r} \left[r^2 \frac{\partial T(r, t)}{\partial r} \right] + \rho_3 c_3 \frac{\partial T(r, t)}{\partial t} = 0, \quad (5.11)$$

thus we find the steady state solution:

$$T_3(r) = \frac{c_5}{r} + c_6. \quad (5.12)$$

We find the constants by applying the boundary conditions.

First applying the boundary condition

$$\left. \frac{dT_1(r)}{dr} \right|_{r=0} = 0, \quad (5.13)$$

we obtain $c_1 = 0$, therefore (5.8) becomes

$$T_1(r) = c_2. \quad (5.14)$$

Then, applying the boundary condition that the temperature outside the nanoparticle needs to reconnect with the laboratory temperature, i.e

$$T_3(r \rightarrow \infty) = T_0, \quad (5.15)$$

we obtain $c_6 = 0$, therefore (5.12) becomes

$$T_3(r) = \frac{c_5}{r} + T_0. \quad (5.16)$$

Now, applying the radial continuity for the core of the nanoparticle

$$T_1(r = a_1) = T_2(r = a_1), \quad (5.17)$$

we obtain that $c_2 = -\frac{qa_1^3}{6K_1} + \frac{c_3}{a_1} + c_4$.

And, applying the radial continuity for the shell of the nanoparticle

$$T_2(r = a_2) = T_3(r = a_2), \quad (5.18)$$

we obtain that $c_5 = -\frac{qa_2^3}{6K_2} + c_3 + c_4a_2 - T_0a_2$.

Therefore, considering the energy conservation which imposes that the total heat power crossing the interface equals the heat power \tilde{Q} delivered by the nanoparticle

$$\oiint \mathbf{j}(\mathbf{r}) \cdot \hat{n} ds = \tilde{Q}. \quad (5.19)$$

Even though our system is a nano-shell, since the local temperature in the core is constant therefore, there will be heat flow only through the outside of the nanoparticle

$$\mathbf{j}(\mathbf{r}) = j(r) \cdot \hat{r}(\theta, \varphi). \quad (5.20)$$

Then, considering that the system has spherical symmetry, then the power that cross the interface of the shell does it in radial direction, hence

$$j(a_2) = \frac{\tilde{Q}}{4\pi a_2^2}. \quad (5.21)$$

Now, considering that the Fourier's law states that the heat flux density vector $\mathbf{j}(\mathbf{r}, t)$, i.e the power per unit area, is proportional to the temperature gradient

$$\mathbf{j}(\mathbf{r}, t) = -K(\mathbf{r})\nabla T(\mathbf{r}, t). \quad (5.22)$$

Therefore, we have

$$j(r) = -K_3\nabla T_3(r), \quad (5.23)$$

$$j(r) = \frac{K_3 c_5}{r^2}. \quad (5.24)$$

Using (5.21) and (5.24) evaluated in $r = a_2$, we obtain $c_5 = \frac{\tilde{Q}}{4\pi K_3}$.

Equating both expressions of c_5 , we find that

$$c_3 = \frac{\tilde{Q}}{4\pi K_3} + \frac{qa_2^3}{6K_2} - c_4 a_2 + T_0 a_2.$$

Then, considering (5.14) therefore $\mathbf{j}(\mathbf{r}) = -K_1\nabla T_1(\mathbf{r}) = 0$, which means that there is no heat flux flowing inside the core. Hence $c_3 = -\frac{qa_1^3}{3K_2}$.

Now, equaling bot expressions of c_3 , we obtain that

$$c_4 = \frac{\tilde{Q}}{4\pi K_3 a_2} + \frac{q}{3K_2} \left(\frac{a_2^2}{2} + \frac{a_1^3}{a_2} \right) + T_0.$$

Substituting c_3 and c_4 in c_2 we got

$$c_2 = \frac{\tilde{Q}}{4\pi K_3 a_2} + \frac{q}{3K_2} \left(\frac{a_2^2}{2} + \frac{a_1^3}{a_2} - \frac{3a_1^2}{2} \right) + T_0.$$

Therefore, considering that the total heat power \tilde{Q} delivered by the nanoparticle is nothing but the integral of q over the spatial domain ν delimited by the volume of the metal shell

$$\iiint q d\nu = \tilde{Q}, \quad (5.25)$$

we obtain that $q = \frac{2\tilde{Q}}{4\pi(a_2^3 - a_1^3)}$.

Replacing q in c_2 , c_3 and c_4 , we finally obtain:

$$T_1(r) = \frac{\tilde{Q}}{4\pi K_3 a_2} \left[1 + \frac{K_3}{K_2} \frac{a_2}{a_2^3 - a_1^3} \left(\frac{a_2^2}{2} + \frac{a_1^3}{a_2} - \frac{3a_1^2}{2} \right) \right] + T_0 \quad (5.26)$$

$$T_2(r) = \frac{\tilde{Q}}{4\pi K_3 a_2} \left[1 + \frac{K_3}{K_2} \frac{a_2}{a_2^3 - a_1^3} \left(\frac{a_2^2}{2} + \frac{a_1^3}{a_2} - \frac{a_1^3}{r} - \frac{r^2}{2} \right) \right] + T_0 \quad (5.27)$$

$$T_3(r) = \frac{\tilde{Q}}{4\pi K_3 r} + T_0 \quad (5.28)$$

Let us first, visualize the temperature inside an outside a gold nano-shell with a silica core with the same size to the gold nanoparticle considered before, i.e $a_2 = 10$ [nm]. Additionally, we will vary the ratio between radius, i.e the amount of gold or the amount of metal.

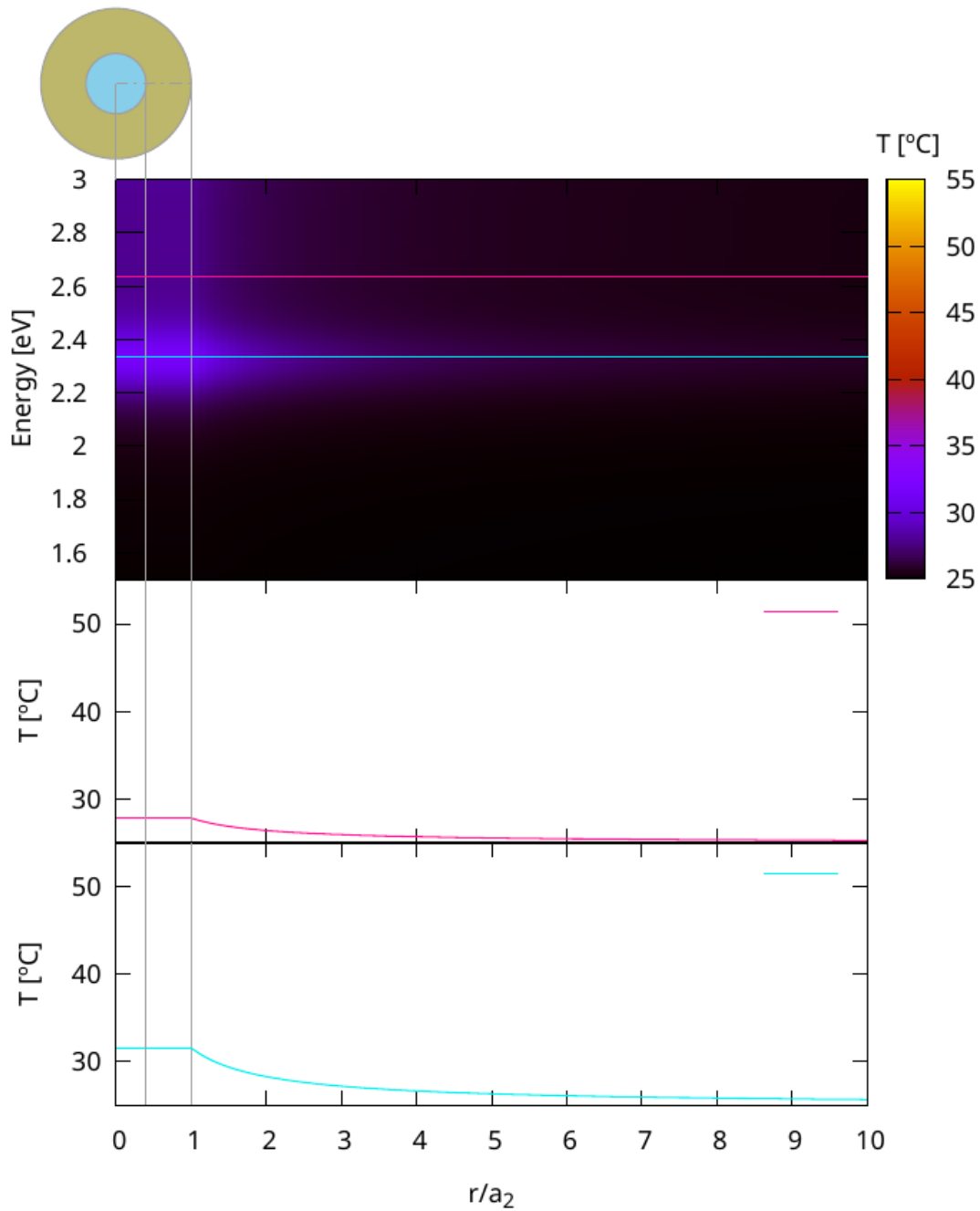


Figure 5.2: Temperature inside and outside a nano-shell particle with silica core embedded by gold with external radius 10 [nm] and $\rho = 0.4$ in the spectrum from 1.5 [eV] to 3 [eV], also we present the temperature in function of the radial distance for 2.63326 [eV] (dark pink line) and 2.33326 [eV] (cyan line)

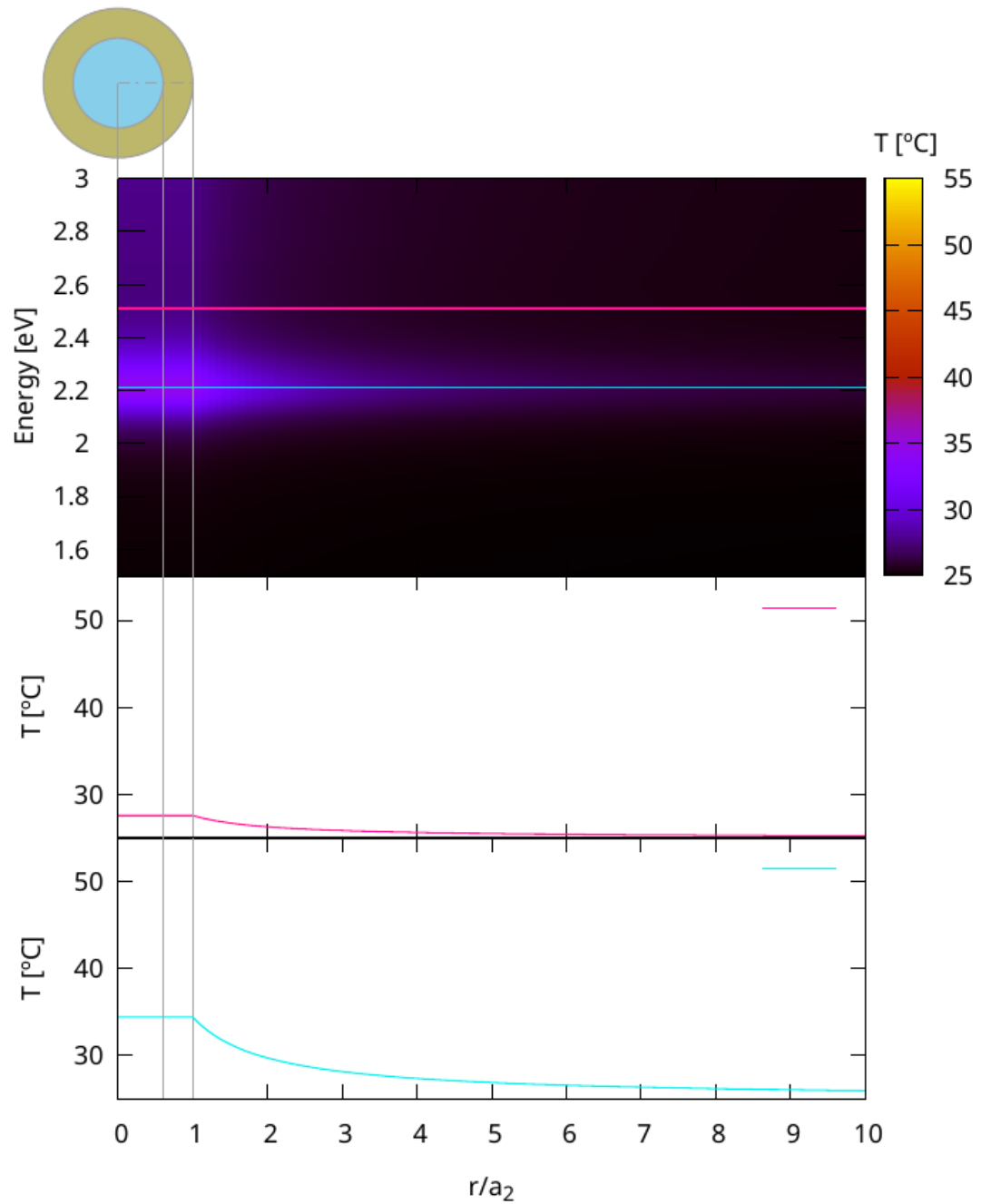


Figure 5.3: Temperature inside and outside a nano-shell particle with silica core embedded by gold with external radius 10 [nm] and $\rho = 0.6$ in the spectrum from 1.5 [eV] to 3 [eV], also we present the temperature in function of the radial distance for 2.50974 [eV] (dark pink line) and 2.20974 [eV] (cyan line)

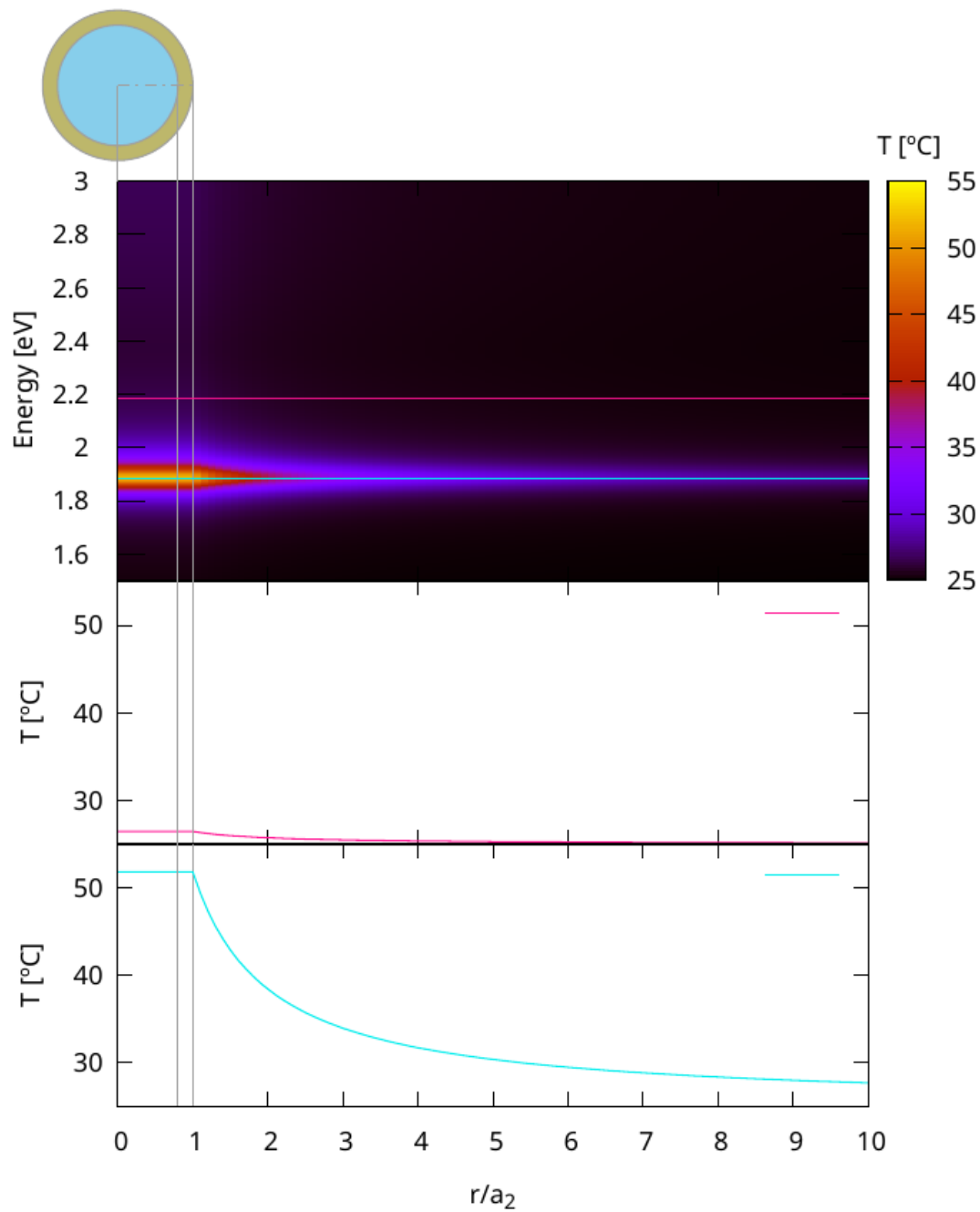


Figure 5.4: Temperature inside and outside a nano-shell particle with silica core embedded by gold with external radius 10 [nm] and $\rho = 0.8$ in the spectrum from 1.5 [eV] to 3 [eV], also we present the temperature in function of the radial distance for 2.18608 [eV] (dark pink line) and 1.88608 [eV] (cyan line)

Based on Figures 5.2, 5.3 and 5.4 we can observe that for nano-shell particles with more metal, i.e lower ρ , the increment of temperature at the resonance is similar to the nanosphere. Meanwhile, by increasing ρ we can achieve higher temperatures without changing the size of the nanoparticle. Also, it is worth to notice that by changing ρ there is a shifting in the place of the spectrum where the resonance occur.

Chapter 6

Trapping behavior

The last chapter of this thesis will be focused in a direct application, which is the trapping behavior of a plasmonic nanoparticle, based on the following work from [26]. In which they use a silica-silver nano-shell with an external radius of 20 [nm] and trapping light with a wavelength in the visible range, to calculate the optical forces within a dipole approximation and expressed in terms of the linear effective complex polarizability, α . In this system the trapping light provides the probe field, exciting the plasmonic resonance of the nanoparticle, leading to express the dipole moment \mathbf{p} of the nanoparticle in the following way

$$\mathbf{p} = \alpha \mathbf{E} \quad (6.1)$$

where \mathbf{E} is the electric field associated with the trapping light. Therefore, the time-average optical force experience by the nano-shell when illuminated by the incident

light is

$$\mathbf{F}_{DA} = \frac{1}{2} \operatorname{Re} \left\{ \sum_i \alpha E_i \nabla E_i^* \right\} \quad (6.2)$$

here E_i are the electric field components. This formula allow us to write the optical force in terms of the extinction cross-section σ_{ext} and the nanoparticle's polarizability α :

$$\mathbf{F}_{DA}(\mathbf{r}) = \frac{n_s \operatorname{Re}\{\alpha\}}{2c\varepsilon_0\varepsilon_s} \nabla I(\mathbf{r}) + \frac{n_s \sigma_{ext}}{c} \mathbf{S} \quad (6.3)$$

where n_s is the solvent refractive index (water in our system, $n_s=1.33$), c is the light velocity, the intensity of the electric field is given by

$$I(\mathbf{r}) = \frac{n_s c |\mathbf{E}(\mathbf{r})|^2}{2}$$

and the time-averaged Poynting vector of the incoming wave is given by

$$\mathbf{S} = \frac{1}{2} \operatorname{Re} \{ \mathbf{E} \times \mathbf{H}^* \}$$

which is related to the light intensity, $|\mathbf{S}| = I(\mathbf{r})$.

The first term of (6.3) is responsible for the particle confinement in optical tweezers and represents the gradient force. Which is conservative since it arises from the potential energy of the induced dipole immersed in the electric field. The second term of (6.3), responsible for the radiation pressure, is the scattering force which is not conservative and is directed along the direction of propagation of the laser beam.

Since we want to describe a trapping behavior, we will work in a configuration aimed to minimize the latter. For this reason, we will model a double-beam OT

in standing wave configuration. This is realized by considering counterpropagating Gaussian beams in paraxial approximation along the z axis, where their waist coincide with the origin of the laboratory reference system. Furthermore, the polarization directions of the two beams are colinear and lie on the xy plane. Hence, the total light intensity, that is a function of the radial, ρ , and axial, z , directions, assumes a standing wave profile:

$$I(\rho, z) = \frac{4I_0w_0^2}{w^2(z)} e^{-\frac{2\rho^2}{w^2(z)}} \cos^2(\Phi(z)) \quad (6.4)$$

where

$$\Phi(z) = k_s z - \zeta(z) + \frac{k_s \rho^2}{2R(z)},$$

such that the wavefront radius is given by

$$R(z) = z \left(1 + \frac{z^2}{z_0^2} \right),$$

and the phase correction is

$$\zeta(z) = \text{atan} \left(\frac{z}{z_0} \right),$$

also the resulting maximum intensity is given by

$$I_0 = \frac{2P}{\pi w_0^2},$$

P is the single Gaussian laser beam power, $w_0 = 0.5[\lambda/NA]$ is the beam waist evaluated by the Abbe criterion, λ is the wavelength in the vacuum, the beam width is

given by

$$w(z) = w_0 \sqrt{1 + \frac{z^2}{z_0^2}},$$

and z_0 is the Rayleigh range which denotes the distance from the beam waist at $z = 0$ to where the beam width has increased by a factor $\sqrt{2}$, so

$$z_0 = \frac{k_s w_0^2}{2}.$$

In (6.4), the interference between the two Gaussian beams generates a standing wave with a modulation of intensity along the z -axis that results in a strong wavelength-dependent modulation of the axial optical force. Therefore, using (6.3) and (6.4) we get an expression of the gradient force components:

$$\langle F \rangle_{DA,\rho}(\rho, z) = -\frac{4 \operatorname{Re}\{\alpha\} I_0 w_0^2 \rho e^{-\frac{2\rho^2}{w^2(z)}}}{c \varepsilon_0 n_s w^4(z)} \left(\cos^2(\Phi(z)) + \frac{z \sin(2\Phi(z))}{k_s w^2(z)} \right) \quad (6.5)$$

$$\begin{aligned} \langle F \rangle_{DA,z}(\rho, z) = & -\frac{4 \operatorname{Re}\{\alpha\} I_0 w_0^2 e^{-\frac{2\rho^2}{w^2(z)}}}{c \varepsilon_0 n_s k_s^2 w^2(z)} \left[\left(1 - \frac{2\rho^2}{w^2(z)} \right) \frac{2z \cos^2(\Phi(z))}{w_0^2 w^2(z)} \right. \\ & \left. + \left(\frac{k_s^2}{4} - \frac{1}{2w^2(z)} - \rho^2 \frac{w^2(z) - 2w_0^2}{w_0^2 w^4(z)} \right) k_s \sin(2\Phi(z)) \right] \end{aligned} \quad (6.6)$$

We will use the spring constants associated with small displacements from the equilibrium trapping point, where the gradient force can be approximated by an harmonic force to characterize the effect of the gain medium on the optical forces. Thus, in the xy transverse plane ($z = 0$), the radiation intensity (6.4) can be approximated as

$$I(\rho) \approx 4I_0 \left(1 - 2\frac{\rho^2}{w_0^2} \right)$$

hence the radial component of the gradient force in (6.3) can be written as

$$\langle F \rangle_{DA,\rho}(\rho) = -\kappa_\rho \rho \quad (6.7)$$

where the trap stiffness is given by

$$\kappa_\rho = \frac{8 \operatorname{Re}\{\alpha\} I_0}{c \varepsilon_0 n_s w_0^2}. \quad (6.8)$$

Correspondingly, along the z axis ($\rho = 0$), the radiation intensity (6.4) can be approximated as

$$I(z) \approx 4I_0 \left[1 - \left(\frac{2z^2}{z_0^2} \right) \left(1 - k_s z_0 + \frac{k_s^2 z_0^2}{2} \right) \right]$$

hence the axial component of the gradient force in (6.3) can be written as

$$\langle F \rangle_{DA,z}(z) = -\kappa_z z$$

where the associated spring constant is given by

$$\kappa_z = \frac{8 \operatorname{Re}\{\alpha\} I_0}{c \varepsilon_0 n_s z_0^2} \left(1 - k_s z_0 + \frac{k_s^2 z_0^2}{2} \right) \quad (6.9)$$

By means of these approximations it is evident the radial and axial components of the force are directly proportional to the real part of the polarizability, α . We can now compare these coefficients with the power absorbed as heat of the particle, which will represent the heat dissipated by the nanoparticle and it is proportional to the real or imaginary part of the same quantity. The effect of the externally pumped gain medium is accounted through the permittivities of the mediums. Furthermore,

since we are working on a 20 [nm] particle we will use the Mie theory to model α and to find the absorption coefficients. This in order to compare the interplay between the gain pumping and the heat dissipated in both cases.

First, for a passive nano-shell i.e $G = 0$ we will increase the laser power in order to visualize the interplay between the optical forces and the heat dissipated by the nanoparticle.

According to Figure 6.1 we can observe that as the power of the laser increase with the purpose to obtain higher optical force, it also increase the power dissipated as heat, which result in higher temperatures. Notice that if the nanoparticle and its surroundings have higher temperatures, even though the optical force is stronger, the efficiency in the trap will be reduced.

In order to obtain higher optical force, we will need to turn on the gain in the active medium. Therefore, we will analyze a gain enhanced nano-shell at the fixed power of $P = 50$ [nm].

According to Figure 6.2 we can observe as the gain pumped to the system increase, and thus the optical force, the maximum of power dissipated as heat is approximate the same. Also, it is worth to notice that there are some regions in which this heat dissipation is reduced, as is evident in the middle and lower rows. Thus, by pumping gain into the system it is possible to obtain higher optical force without having an massive increased on the heat dissipated by the nanoparticle.

Now, considering a fixed wavelength of $\lambda = 580$ [nm] in which we can observe more clearly the relationship between the gain pumped to the system, the laser power

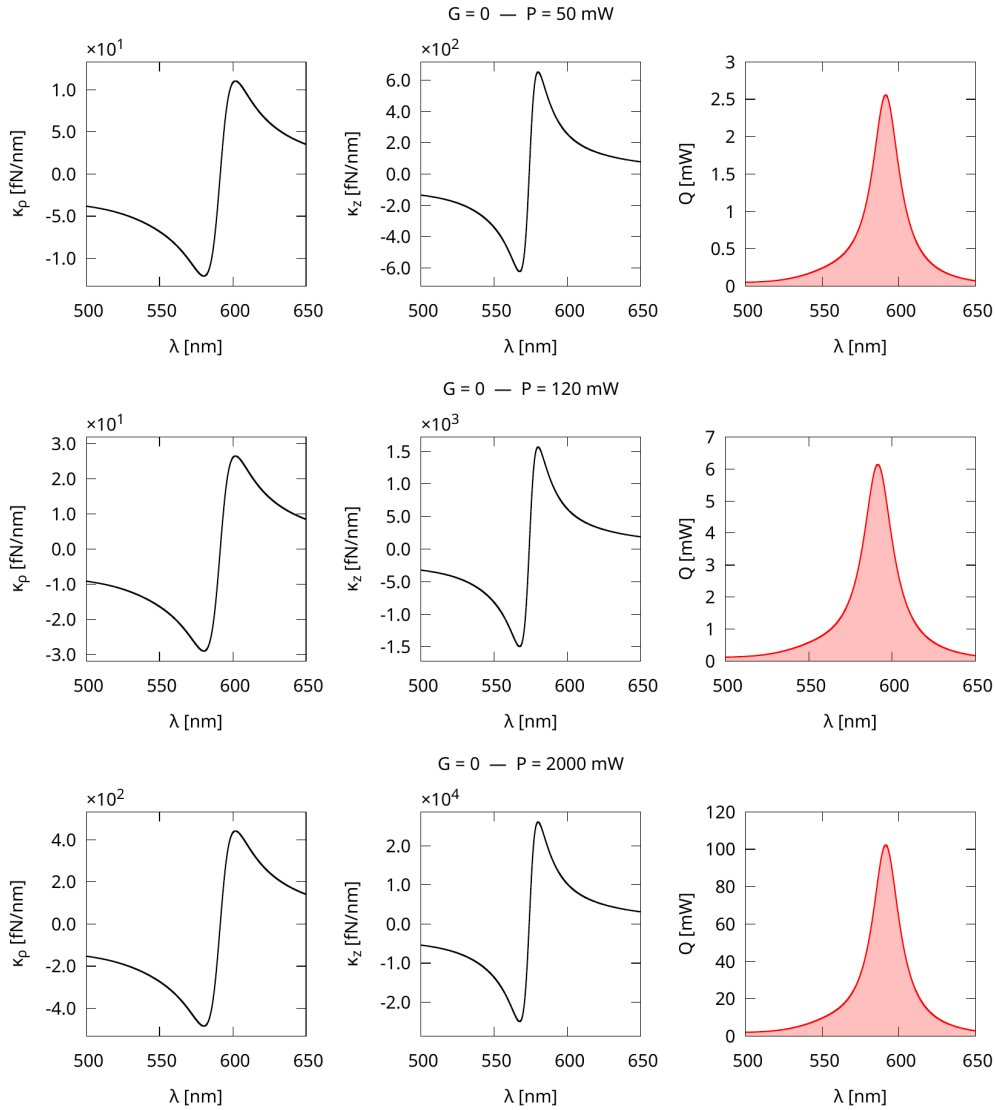


Figure 6.1: Radial and axial components of the optical force, power dissipated as heat of a passive silica-silver nano-shell of radius $a_2 = 20 \text{ [nm]}$ for $P = 50 \text{ [mW]}$ (upper row), $P = 120 \text{ [mW]}$ (middle row) and $P = 2000 \text{ [mW]}$ (lower row).

and the heat dissipated by the nanoparticle. According to Figure 6.3 we can observe that it is possible of obtain the same amount of optical force with a minimum heat dissipated by injecting the appropriate amount of gain into the system.

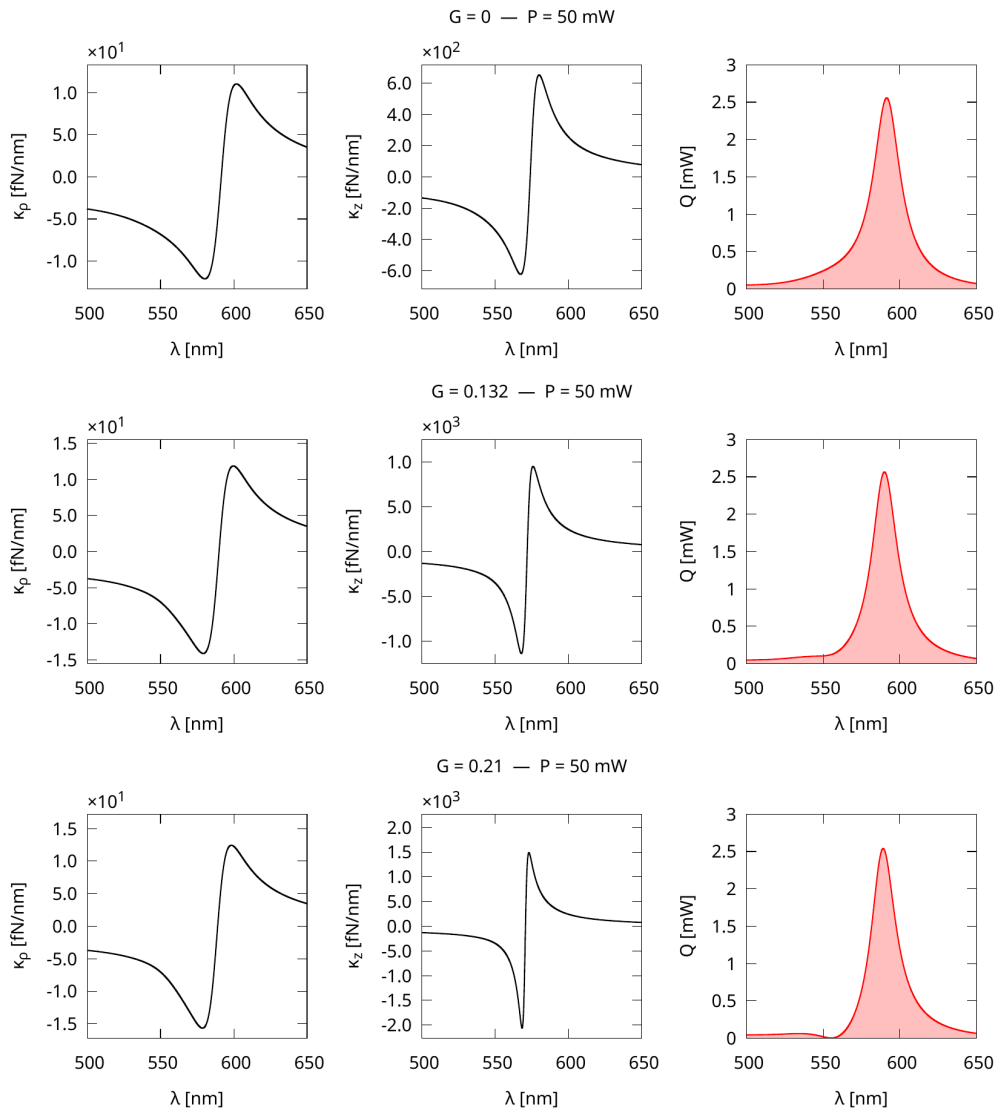


Figure 6.2: Radial and axial components of the optical force, power dissipated as heat of a gain enhanced silica-silver nano-shell at $P = 50$ [mW] for $G = 0$ (upper row), $G = 132$ (middle row) and $G = 0.21$ (lower row).

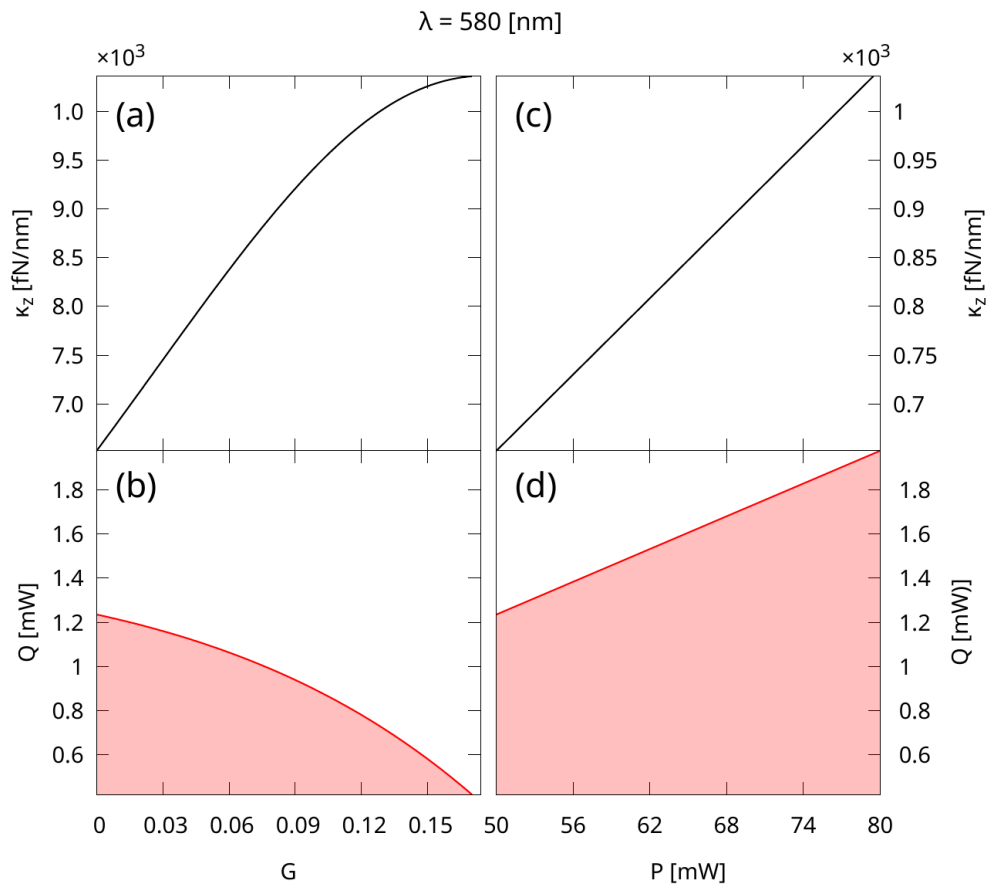


Figure 6.3: Axial component of the optical force related to the heat dissipated by the nanoparticle as we increase the gain pumped to the system, (a) and (b), and the power of the laser, (c) and (d).

Chapter 7

Conclusions

The comparison between the quasistatic approximation and the Mie theory by the theoretical analysis of the absorption cross section has lead us to the conclusion that in nano-shell particles the quasistatic regime breaks not only when the size of the particle is increased, but also when gain is pumped into the system. Additionally it is worth to consider that this point of breakage also depends on the amount of metal that has the nanoparticle, i.e the ratio between radius.

Considering that in this study we are working with gain enhanced metal nano-shells we have applied the Mie theory for the electromagnetic response in the characterization of the thermal behavior. Based on the Baffou model for the temperature inside and outside the nanoparticle we have successfully extended it for the nano-shell particle. Obtaining that when comparing a nanosphere and a nano-shell particle of the same size, by changing the ratio between radius of the nano-shell particle the increment of temperature is significantly bigger.

This model was applied for the analysis of the efficiency of an optical trap. As result, we obtain higher optical forces by pumping gain into the nano-shell particle than by increasing the laser power of the trap.

This thesis contains a complete characterization of the temperature in a system that consist of a plasmonic nano-shell particle and its surrounding medium, which is relevant for applications like Plasmonic Photothermal Therapy.

Bibliography

- [1] Abdoon, A. S., Al-Ashkar, E. A., Kandil, O. M., Shaban, A. M., Khaled, H. M., El Sayed, M. A., El Shaer, M. M., Shaalan, A. H., Eisa, W. H., Eldin, A. A., et al. (2016). *Efficacy and Toxicity of Plasmonic Photothermal Therapy (Ppvt) Using Gold Nanorods (Gnrs) Against Mammary Tumors in Dogs and Cats*. *Nanomedicine* 2016, 12, 2291-2297.
- [2] Ali, M. R., Ibrahim, I. M., Ali, H. R., Selim, S. A., and El-Sayed, M. A. (2016). *Treatment of Natural Mammary Gland Tumors in Canines and Felines Using Gold Nanorods-Assisted Plasmonic Photothermal Therapy to Induce Tumor Apoptosis*. *Int. J. Nanomed.* 2016, 11, 4849-4863.
- [3] Antuofermo, E., Miller, M. A., Pirino, S., Xie, J., Badve, S., and Mohammed, S. I. (2007). *Spontaneous Mammary Intraepithelial Lesions in Dogs-a Model of Breast Cancer*. *Cancer Epidemiol., Biomarkers Prev.* 2007, 16, 2247-56.
- [4] Baburin, A., Merzlikin, A., Baryshev, A., Ryzhikov, I., Panfilov, Y., and Rodionov, I. (2019). *Silver-based plasmonics: golden material platform and application challenges*. *Optical Materials Express.* 9. 611.

- [5] Baffou, G., Cichos, F., and Quidant, R. (2020). *Applications and Challenges of Thermoplasmonics*. Nature Materials.
- [6] Baffou, G., and Quidant, R. (2022). *Thermo-plasmonics: using metallic nanostructures as nano-sources of heat*. Laser & Photonics Review 7, No. 2, 171-187(2013).
- [7] Bayda, S., Adeel, M., Tuccinardi, T., Cordani, M., and Rizzolio, F. (2019). *The History of Nanoscience and Nanotechnology: From Chemical–Physical Applications to Nanomedicine*. Molecules, 25(1), 112.
- [8] Bohren, C. F., Huffman, D. R. (2008). *Absorption and Scattering of Light by Small Particles*. John Wiley and Sons.
- [9] Caicedo, K., Cathey, A., Infusino, M., Aradian, A., and Veltri, A. (2022). *Gain-driven singular resonances in active core-shell and nano-shell plasmonic particles*. Journal of the Optical Society of America B, 39, 107-116.
- [10] Cerdán, L. and Manjavacas, A. (2023). *Analysis of the Limits of the Optical Response of a Metallic Nanoparticle with Gain* The Journal of Physical Chemistry C, 127, 2371.
- [11] Cherukuri, P., Glazer, E. S., and Curley, S. A. (2010). *Targeted Hyperthermia Using Metal Nanoparticles*. Adv. Drug Deliv. Rev., 62, 339–345.
- [12] Gillibert, R., Colas, F., de La Chapelle, M. L., and Gucciardi, P. G. (2020). *Heat Dissipation of Metal Nanoparticles in the Dipole Approximation*. Springer
- [13] Hirsch, L. R., Stafford, R. J., Bankson, J. A., Sershen, S. R., Rivera, B., Price, R. E., ... West, J. L. (2003). *nano-shell-mediated near-infrared thermal therapy of*

- tumors under magnetic resonance guidance*. Proceedings of the National Academy of Sciences, 100(23), 13549–13554.
- [14] Jackson, J. D. (1999) *Classical Electrodynamics*. John Wiley and Sons.
- [15] Johnson, P. B., and Christy, R. W. (1972). *Optical Constants of the Noble Metals*. Physical Review B, (6), 4370-4379.
- [16] Kuppe, C., Rusimova, K. R., Ohnoutek, L., Slavov, D., Valev, V. K. (2020) *"Hot" in Plasmonics: Temperature-Related Concepts and Applications of Metal Nanostructures* Advance Optical Materials.
- [17] Lal, S., Clare, S. E., and Halas, N. J. (2008). *nano-shell-Enabled Photothermal Cancer Therapy: Impending Clinical Impact*. Acc. Chem. Res., 41, 1842.
- [18] Lim, Z. Z. J., Li, J. E. J., Ng, C. T., Yung, L. Y. L., and Bay, B. H. (2011). *Gold Nanoparticles in Cancer Therapy*. Acta Pharmacol. Sin., 32, 983–990.
- [19] Macewen, E. (1990). *Spontaneous Tumors in Dogs and Cats - Models for the Study of Cancer Biology and Treatment*. Cancer Metastasis Rev. 1990, 9, 125-136
- [20] Maier, S. A. (2007). *Plasmonics: Fundamentals and Applications*. Springer.
- [21] Mishchenko, M. I., Travis, L. D., and Mackowski, D. W. (1996). *T-matrix computations of light scattering by nonspherical particles: A review*. Journal of Quantitative Spectroscopy and Radiative Transfer, 55(5), 535–575.
- [22] Moustafa, R. K. A., Yue, W. and Mostafa, A. E. (2019). *Gold-Nanoparticle-Assisted Plasmonic Photothermal Therapy Advances Toward Clinical Application*. J. Phys. Chem. C 2019, 123, 15375-15393.

- [23] Novotny, L., and Hecht, B. (2006). *Principles of Nano-Optics*. Cambridge University Press.
- [24] Oleson, J. R., and Dewhirst, M. W. (1983). *Hyperthermia: An Overview of Current Progress and Problems*. *Current Problems in Cancer*, 8(6), 1–62.
- [25] Olver, P. J. (2014) *Introduction to Partial Differential Equations*. Undergraduate Texts in Mathematics.
- [26] Polimeno, P., Patti, F., Inlusino, M., Sánchez, J., Iatì, M. A., Saija, R., Volpe, G., Maragò, O. M., Veltri, A. (2020). *Gain-Assisted Optomechanical Position Locking of Metal/Dielectric Nanoshells in Optical Potentials* *ACS Photonics* 2020, 7, 1262-1270.
- [27] Recalde, N., Bustamante, D., Infusino, M., and Veltri, A. (2023). *Dynamic Multi-Mode Mie Model for Gain-Assisted Metal Nano-Spheres* *Materials* 16, 10.3390.
- [28] Sapareto, S. A., and Dewey, W. C. (1984). *Thermal Dose Determination in Cancer Therapy*. *Int. J. Radiation Oncology Biol. Phys.*, 10, 787–800.
- [29] Schwartz, J. A., Shetty, A. M., Price, R. E., Stafford, R. J., Wang, J. C., Uthamantil, R. K., Pham, K., McNichols, R. J., Coleman, C. L., and Payne, J. D. (2009). *Feasibility Study of Particle-Assisted Laser Ablation of Brain Tumors in Orthotopic Canine Model*. *Cancer Res.* 2009, 69, 1659-1667.
- [30] Urban, S. U., Carretero-Palacios, S., Andrey, A. L., Lohmuller, T., Feldmann, J., and Jackel, F. (2014). *Optical trapping and manipulation of plasmonic nanoparticles: fundamentals, applications, and perspectives* *Nanoscale*, 2014, 6, 4458

- [31] Veltri, A., and Ashod, A.(2012).*Optical response of a metallic nanoparticle immersed in a medium with optical gain* Physical Review B, 85(11).
- [32] Veltri, A., Chipouline, A., and Aradian, A. (2016).*Multipolar, time-dynamical model for the loss compensation and lasing of a spherical plasmonic nanoparticle spaser immersed in an active gain medium*. Scientific Reports, 6(1).
- [33] Zhang, Y., Min, Ch., Dou, X., Wang, X., Urbach, H. P., Somekh, M., and Yuan, X. (2021). *Plasmonic tweezers: for nanoscale optical trapping and beyond*. Light Sci Appl, 59 (2021).